Aeroacoustic noise suppression and aerodynamic robustness in owl-inspired leading-edge serrations

January 2019

Chen Rao

Graduate School of Engineering

Chiba University

Aeroacoustic noise suppression and aerodynamic robustness in owl-inspired leading-edge serrations

January 2019

Chen Rao

Graduate School of Engineering

Chiba University

Contents

Abstract

Owls are a master to achieve silent flight in gliding and flapping flights under natural turbulent environments owing to their unique wing morphologies, normally characterized by leading-edge serrations, trailing-edge fringes and velvet-like surfaces. How these morphological features affect aerodynamic force production and aeroacoustic noise suppression is of significance for aerodynamic / aeroacoustic control in biomimetic designs of owl-inspired adaptations for various fluid machineries. In this study, aiming at providing a comprehensive understanding of the underlying serration-based aeroacoustic mechanisms, we address a large-eddy simulation (LES)-based study of owl-inspired single feather wing models with and without leading-edge serrations over a broad range of angles of attack (AoAs) from 0° to 20°.

As our first step to investigate the essential mechanisms of the leading-edge serrations in steady flow condition, we pay specific attention to the aerodynamic characteristics of the single-feather models traveling in uniform incoming flow. Our results show that leading-edge serrations can passively control the laminar-turbulent transition over the upper wing surface, and hence stabilize the suction flow. The mechanisms is likely achieved by the leading-edge serrations, which, as a flow filter, break up the leading-edge vortex into numbers of small eddies and suppress the KH instability within the separated shear layer. We also find that there exists a tradeoff between force production and turbulent flow control (i.e. aeroacoustic control): poor at lower AoAs but capable of achieving equivalent aerodynamic performance at higher AoAs > 15° compared to the clean model.

Furthermore, through mimicking wind-gusts under a longitudinal fluctuation in free-stream inflow and a lateral fluctuation in pitch angle, we continue our LES-based study to investigate the aerodynamic robustness to wind-gust associated with the owl-inspired leading-edge serrations. Based on the simulated results, it is revealed that the serrated model is capable of dynamically suppressing the turbulent instability and aerodynamic force fluctuations. The serration-based passive flow control mechanisms and the tradeoff are confirmed independently to the perturbed inflow and fluctuated pitch motion, demonstrating the aerodynamic robustness in wind-gust associated with the leading-edge serrations.

Our results reveal that the owl-inspired leading-edge serrations can be a robust micro-device for aeroacoustic control coping with unsteady and complex wind environments in biomimetic rotor designs for various fluid machineries.

List of figures

Figure 5-17. Transient characteristics in pitch disturbance. (A) Time-varying pitch angles with steady ($\alpha = 0°$) and unsteady ($\alpha = 1°$, $\alpha = 2°$) phases, time courses of lift (B) and drag (C) coefficients, as well as lift-to-drag ratios (D) associated with clean (blue) and serrated (red) leading-edge wing models at $\Phi_0 = 5°$ in steady (solid lines) and unsteady (dashed, dotted lines) state, respectively.

Figure 5-18. Transient characteristics in pitch disturbance. (A) Time-varying pitch angles with steady ($\alpha = 0°$) and unsteady ($\alpha = 1°$, $\alpha = 2°$) phases, time courses of lift (B) and drag (C) coefficients, as well as lift-to-drag ratios (D) associated with clean (blue) and serrated (red) leading-edge wing models at $\Phi_0 = 15°$ in steady (solid lines) and unsteady (dashed, dotted lines) state, respectively.

List of tables

1. Introduction

1.1 Background - The silent flight of the owl

Owls are a master to achieve silent flight [1-9] in gliding and flapping flights even under natural turbulent environments. Unlike most bird hunters who fly faster than their prey during hunting, the owls develop a unique and sophisticated hunting strategy relies on the silent flight as shown in figure 1-1.

Figure 1-1. Sophisticated silent hunting skill performed by the owl. (Photograph by Tom Samuelson)
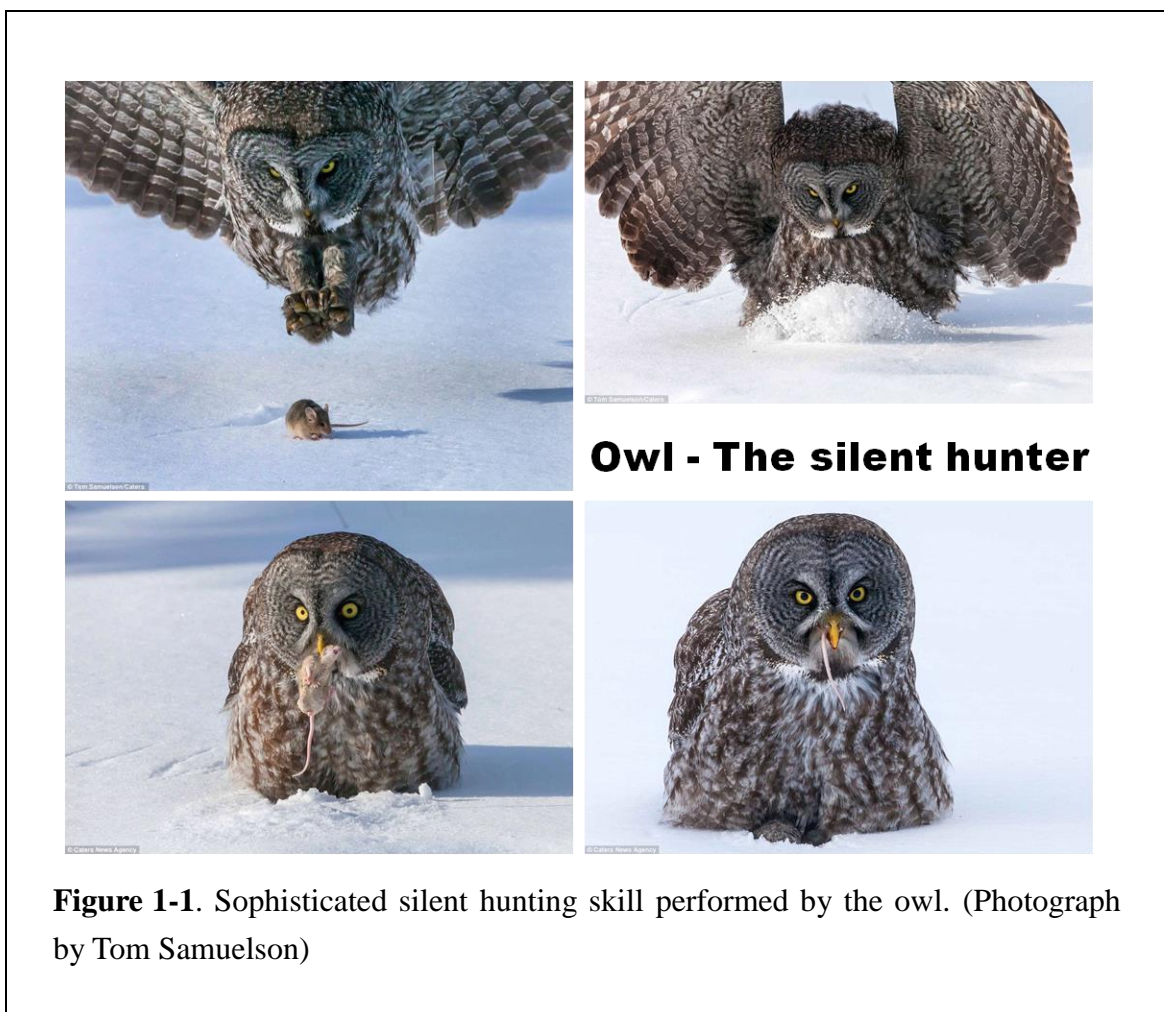
Some species of owl, including the barn owl (*Tyto alba*) and the barred owl (*Strix varia*), can suppress the wing-induced aerodynamic sound to an extremely lower level of a frequency below 2 kHz during gliding or flapping flight [4] owing to their unique wing morphologies that evolved after a long period of evolution, which are normally

characterized by leading-edge serrations, trailing-edge fringes and velvet-like surfaces as illustrated in figure 1-2. The silent flight allows them to be capable of attacking prey like mice and voles easily. Such aerodynamic sound suppression is achieved even below the hearing ranges of owls themselves [4], which is also important for them to refrain from distracting because owls require extreme concentration on their bi-aural hearing systems to localize prey during flight.
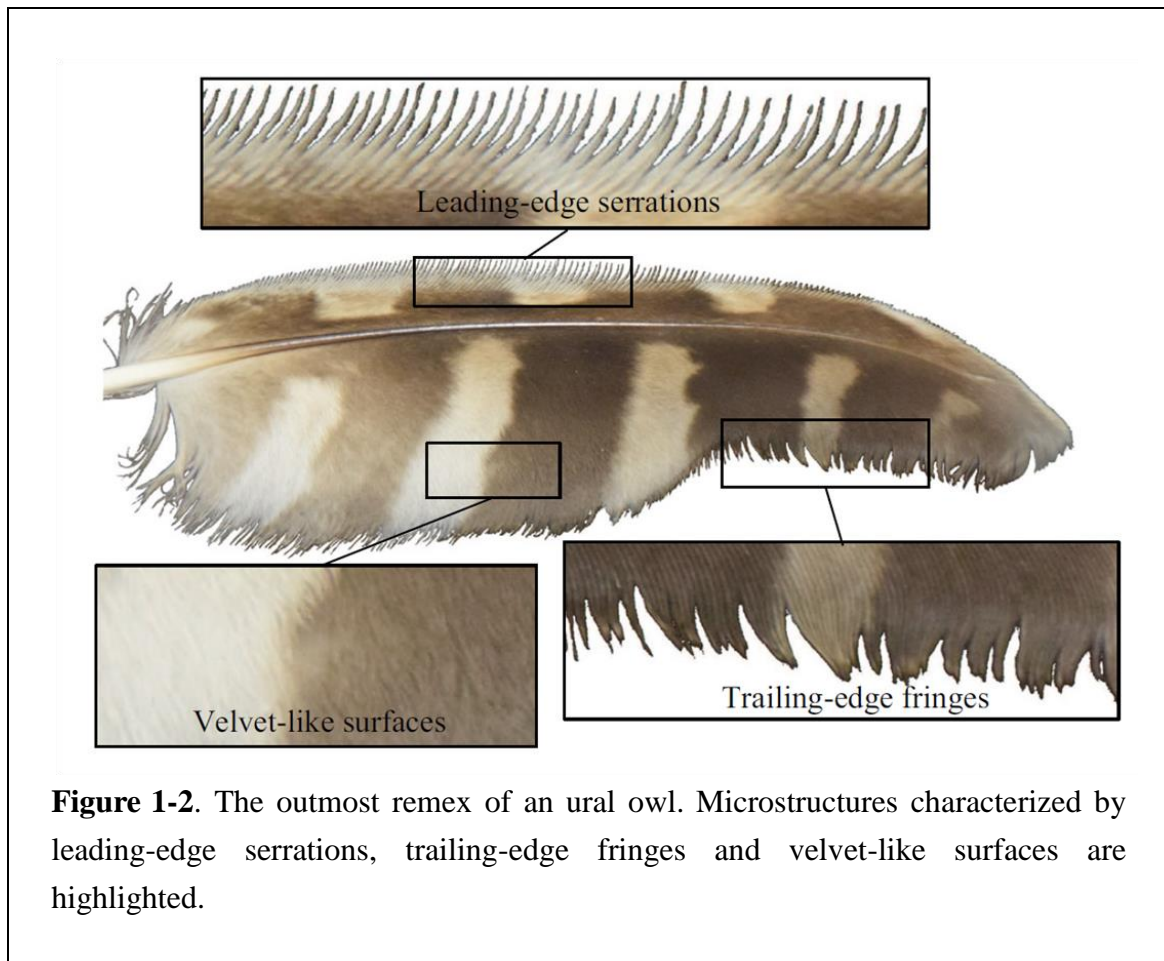
Figure 1-2. The outmost remex of an ural owl. Microstructures characterized by leading-edge serrations, trailing-edge fringes and velvet-like surfaces are highlighted.

The robust mechanisms associated with silent owl flight have therefore considerable potential for shedding light on bringing an innovative biomimetic design or improving the technologies of noise reduction in blades or rotors of wind turbines, aircrafts as well as multi-rotor drones [10-17].

1.2 Literature review

Graham [1] first reported that most species of owl evolved a unique wing structure

with adaptations such as the comb-like serrations at leading-edge, fringes at trailing-edge and a velvety wing surface. Kroeger et al. [3] later demonstrated experimentally that without leading-edge serrations and trailing-edge fringes, the modified owl wings emitted sounds as noisy as other birds with a similar body mass did while flying at a similar speed. Recently, acoustic measurements on live owls [5, 7] or realistic owl wing specimens [8, 9] also demonstrated the sound suppression characteristics compared with non-silent species (without the specified microstructures) or non-serrated wings.

Meanwhile, the idea of equipping owl-inspired artificial serrations onto the leading-edge of airfoils or rotor blades has been frequently investigated [10-17]. All attempts demonstrated the beneficial effect of the leading-edge serrations on noise reduction especially at higher frequencies. Furthermore, recent numerical analysis also identified the mitigation of far-field overall sound pressure level (OASPL) via leading-edge serrations for a rod-airfoil configuration [18]. However, the serration-based aerodynamic performance could not reach an agreement. Sodermann [13] indicated that the serrations, when placed properly on the airfoil, could increase maximum lift and angle of attack for maximum lift, decrease the drag at large angles of attack. Collins [15] also proved that the leading-edge serrations yield improved low-speed performance of the NACA 2412 and NACA 0015 airfoils over the Reynolds number range of $2 \sim 5 \times 10^5$. In contrast, Arndt et al. [12] reported that the serrations alter the pressure distribution over the blade and the variation in blade loading apparently decreases the overall efficiency of the rotor. While Soderman [14] found the rotor performance is essentially unchanged by the presence or absence of serrations on the blades. Ito [16] additionally concluded that the aerodynamic characteristics of the serrated airfoils have a strong Reynolds number effect.

While being a long-standing problem that the unique owl-wing morphologies show apparent association with sound suppression and aerodynamic force production, it remains unclear how the leading-edge serrations correlate with the aeroacoustic mechanisms. Bachmann et al. [19] presented a study of morphometric characterization of wing feathers of the barn owl, including characteristics and morphology of feathers, barbs, radiates in detail. A specific focus was given on the comb-like serrations, which could merely be found in very few feathers that form the distal part of the wing's leading-edge. They reported that each serration was indeed the tip of a single barb, having a very complicated 3D shape, and the size and orientation of the serration differed depending on its spanwise position. Bachmann et al. [19] also reported that owls have much larger wing

areas compared to pigeon with the same body mass, which results in a reduced wing loading. This allows owls to glide at a relative lower speed of 2.5 ~ 7.5 m/s [20] while approaching the prey, and hence prevents extra noise emission. However, around a wing moving at the lower Reynolds numbers of owl flight, i.e. 20000 < Re < 80000 based on a chord length of approximately 150 mm, an inevitable separation bubble or leading-edge vortex is normally observed on the suction surface due to laminar-turbulent transition. This bubble or leading-edge vortex varies in shape and strength dependent upon moving velocities and angles of attack, normally enhancing aerodynamic noise production. And the unsteadiness of the separation bubble may lower the aerodynamic performance in flight maneuvers. Therefore, in addition to the general wing morphology and geometry, owls further require some novel flow control mechanisms, likely by using their unique wing structures to stabilize the suction surface flow and hence achieve silent flight.

Bachmann et al. [21] further investigated the 3D characterization of natural serrations and reconstructed a highly approximated serration model for biomimetic applications based on quantitative morphometric data. Klän et al. [22] digitized natural wings through the scanning 3D surface of dead owls and reconstructed geometric wing models to yield a smooth surface while fixing the increased camber based on drying or narcotizing of the birds. They then built up a clean wing model and used it as a reference case resembling the basic wing geometry. Aerodynamic characteristics of the artificial models were then studied through particle-image velocimetry (PIV) and force measurements, for both clean and serrated wing models in a wind tunnel [20, 23]. It was found that, at lower angles of attack ($0° \leqslant \mathrm{AoA} \leqslant 6°$), the serrations seemed to stabilize the flow by passively controlling the boundary layer and separation bubble, but the artificial leading-edge serrations obviously lowered the aerodynamic performance compared to a clean model.

1.3 Objectives of this thesis

As known the micro-structured fluid dynamics can play a significant role in controlling boundary layer [24], and the leading-edge serrations likely provide a tradeoff between aerodynamic force production and sound suppression [20, 23], hence play a crucial role in achieving silent flight of owls. However, the essential underlying mechanisms, such as how the serrated-structures influence the flow separations (or instability) and how this affects the force production, remain unclear so far. In this thesis, aiming at providing a comprehensive understanding of the underlying serration-based

aeroacoustic phenomenon, we herein address an integrated study by combining low-speed wind tunnel experiments and computational fluid dynamic (CFD) modeling with owl-inspired single-feather wing models.

1.4 Outline of this thesis

The outline of this thesis is organized as follow:

In chapter 2, we introduce the experimental owl-inspired single-feather wing models which were artificially fabricated based on the outermost remex of realistic owl wing with serrated leading-edge. The experiments of particle-image velocimetry (PIV) and force measurements in low-speed wind tunnel are briefly introduced.

In chapter 3, we further introduce two idealized numerical models for CFD modeling. The computational domain and grids, as well as the LES-based CFD solver for transient flow fields and acoustic solver for near-field noise spectra are presented.

In chapter 4, a verification study of mesh independency is given. The CFD modeling is further validated through a comprehensive comparison with PIV measurements. Then, based on the simulated flow structures and velocity spectra, sound spectra, as well as aerodynamic forces, we give an extensive discussion on how the serrations are capable of passively controlling laminar-turbulent transition and suppressing the vortex shedding-induced instability and hence sound emission, as well as their correlations with aerodynamic performance.

In chapter 5, motivated by the sophisticated maneuvering and silent flight that owls can achieve even while coping with natural turbulent environments, we further conducted a computational study of aerodynamic robustness in owl-inspired leading-edge serrations with the LES-based CFD solver. Two conceptual wind-gust models were employed to mimic perturbed inflow and fluctuated pitch motion. Based on the simulated results, we give an extensive discussion on the aerodynamic robustness associated with the capability of the leading-edge serrations in passively controlling laminar-turbulent transition as well as their correlations with aerodynamic performance under perturbed inflow and fluctuated pitch motion.

In chapter 6, we make general conclusions of this study.

References

[1] Graham RR 1934 The silent flight of owls. *Journal of the Royal Aeronautical Society*. **38** 837-843. (http://dx.doi.org/10.1017/S0368393100109915)

[2] Gruschka HD, Borchers IU and Coble JG 1971 Aerodynamic noise produced by a gliding owl. *Nature*. **233** 409-411. (http://dx.doi.org/10.1038/233409a0)

[3] Kroeger RA, Grushka HD and Helvey TC 1972 Low speed aerodynamics for ultra-quiet flight. *Final Technical Report (July 1970 – May 1971) Tennessee Univ Space Inst Tullahoma* (http://www.dtic.mil/docs/citations/AD0893426)

[4] Lilley GM 1998 A study of the silent flight of the owl. *4th AIAA/CEAS Aeroacoustics Conference, Toulouse, AIAA Paper*. **2340** 1-6. (http://dx.doi.org/10.2514/6.1998-2340)

[5] Chen K, Liu Q, Liao G, Yang Y, Ren L, Yang H and Chen X 2012 The sound suppression characteristics of wing feather of owl (*Bubo bubo*). *Journal of Bionic Engineering*. **9** 192-199. (http://dx.doi.org/10.1016/S1672-6529(11)60109-1)

[6] Wagner H, Weger M, Klaas M and Schröder W 2017 Features of owl wings that promote silent flight. *Interface Focus* **7** 20160078. (http://dx.doi.org/10.1098/rsfs.2016.0078)

[7] Sarradj E, Fritzsche C and Geyer T 2011 Silent owl flight: Bird flyover noise measurements. *AIAA Journal*. **49** 769-779. (http://dx.doi.org/10.2514/1.J050703)

[8] Geyer T, Sarradj E and Fritzsche C 2012 Silent owl flight: Acoustic wind tunnel measurements on prepared wings. *18th AIAA/CEAS Aeroacoustics Conference (33rd AIAA Aeroacoustics Conference), Colorado Springs, AIAA Paper*. **2230** 1-17. (http://dx.doi.org/10.2514/ 6.2012-2230)

[9] Geyer T, Claus VT, Sarradj E and Markus PM 2016 Silent owl flight: The effect of the leading edge comb on the gliding flight noise. *22nd AIAA/CEAS Aeroacoustics Conference, Lyon, AIAA Paper*. **3017** 1-12. (http://dx.doi.org/10.2514/6.2016-3017)

[10] Hersh AS and Hayden RE 1971 Aerodynamic sound radiation from lifting surfaces with and without leading-edge serrations. *NASA-CR-114370*.

[11] Hersh AS, Soderman PT and Hayden RE 1974 Investigation of acoustic effects of leading-edge serrations on airfoils. *Journal of Aircraft*. **11** 197-202. (http://dx.doi.org/10.2514/3.59219)

[12] Arndt REA and Nagel RT 1972 Effect of leading edge serrations on noise radiation from a model rotor. *Society of Naval Architects and Marine Engineers, and U.S.*

Navy, Advanced Marine Vehicles Meeting, Annapolis, AIAA Paper. **655**. (http://dx.doi.org/10.2514/6.1972-655)

[13] Soderman PT 1972 Aerodynamic effects of leading-edge serrations on a two-dimensional airfoil. *NASA TECHNICAL MEMORANDUM X-2643*.

[14] Soderman PT 1973 Leading edge serrations which reduce the noise of low-speed rotors. *NASA TECHNICAL NOTE D-7371*.

[15] Collins FG 1981 Boundary-layer control on wings using sound and leading-edge serrations. *AIAA Journal*. **19** 129-130. (http://doi.org/10.2514/3.50930)

[16] Ito S 2009 Aerodynamic influence of leading-edge serrations on an airfoil in a low Reynolds number - A study of an owl wing with leading edge serrations -. *Journal of Biomechanical Science and Engineering*. **4** 117-123. (http://dx.doi.org/10.1299/jbse.4.117)

[17] Narayanan S, Chaitanya P, Haeri S, Joseph P, Kim JW and Polacsek C 2015 Airfoil noise reductions through leading edge serrations. *Physics of Fluids*. **27** 1-17. (http://dx.doi.org/10.1063/1.4907798)

[18] Agrawal BR and Sharma A 2016 Numerical analysis of aerodynamic noise mitigation via leading edge serrations for a rod-airfoil configuration. *International Journal of Aeroacoustics*. **15** 734-756. (http://doi.org/10.1177/1475472X16672322)

[19] Bachmann T, Klän S, Baumgartner W, Klaas M, Schröder W and Wagner H 2007 Morphometric characterisation of wing feathers of the barn owl *Tyto alba pratincola* and the pigeon *Columba livia*. *Frontiers in Zoology*. **4** 1-15. (http://dx.doi.org/10.1186/1742-9994-4-23)

[20] Winzen A, Roidl B, Klän S, Klaas and M, Schröder W 2014 Particle-image velocimetry and force measurements of leading-edge serrations on owl-based wing models. *Journal of Bionic Engineering*. **11** 423-438. (http://dx.doi.org/10.1016/S1672-6529(14)60055-X)

[21] Bachmann T and Wagner H 2011 The three-dimensional shape of serrations at barn owl wings: towards a typical natural serration as a role model for biomimetic applications. *Journal of Anatomy*. **219** 192-202. (http://dx.doi.org/10.1111/j.1469-7580.2011.01384.x)

[22] Klän S, Bachmann T, Klaas M, Wagner H and Schröder W 2009 Experimental analysis of the flow field over a novel owl based airfoil. *Experiments in Fluids*. **46** 975-989. (http://dx.doi.org/10.1007/s00348-008-0600-7)

[23] Klän S, Klaas M and Schröder W 2010 The influence of leading-edge serrations on the flow field of an artificial owl wing. *28th AIAA Applied Aerodynamics*

Conference, Chicago, AIAA Paper. **4942** 1-9.
(http://dx.doi.org/10.2514/6.2010-4942)

[24] Liu H, Kolomenskiy D, Nakata T and Li G 2017 Unsteady bio-fluid dynamics in flying and swimming. *Acta Mechanica Sinica*. **33** 663-684.
(http://doi.org/10.1007/s10409-017-0677-4)

2. An owl-inspired single-feather wing model

2.1 The wing and feathers of realistic owl
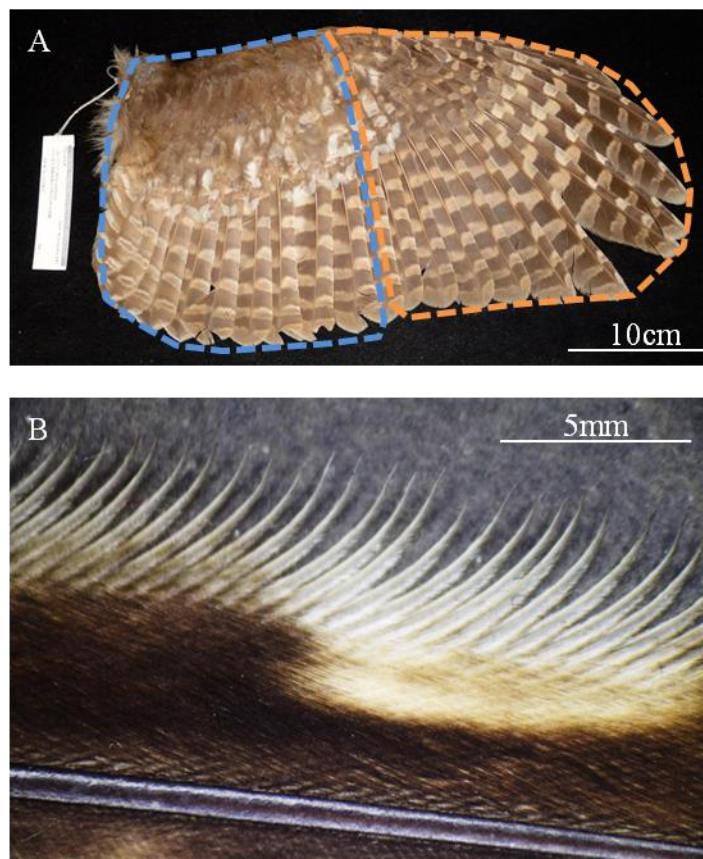
Figure 2-1. (A) Right wing of a female Ural owl (*Strix uralensis*). The arm and hand wings are highlighted by cyan and orange dashed line, respectively. (B) The comb-like serrated leading-edge at the vane of the outermost remex.

Figure 2-1(A) shows the right wing of a female Ural owl (*Strix uralensis*). The specimen was collected in Iwate Prefecture, Japan and kindly provided by Yamashina Institute for Ornithology. The owl's wing consists of an arm-wing (colored cyan) and a hand-wing (colored orange). The arm-wing is structured by bones and muscles, and

covered by velvety coverts that densely overlapped on the skin, forming a rounded leading-edge. The hand-wing is made up of remiges (or flight feathers) only with sharp leading- and trailing-edge. The vane of the outermost remex shows a comb-like serrated leading-edge as illustrated in figure 2-1(B). The second outermost remex has smaller serrations on its vane, overlapping with adjacent feathers to form a continuous wing surface, which acts as a secondary serrated leading-edge.
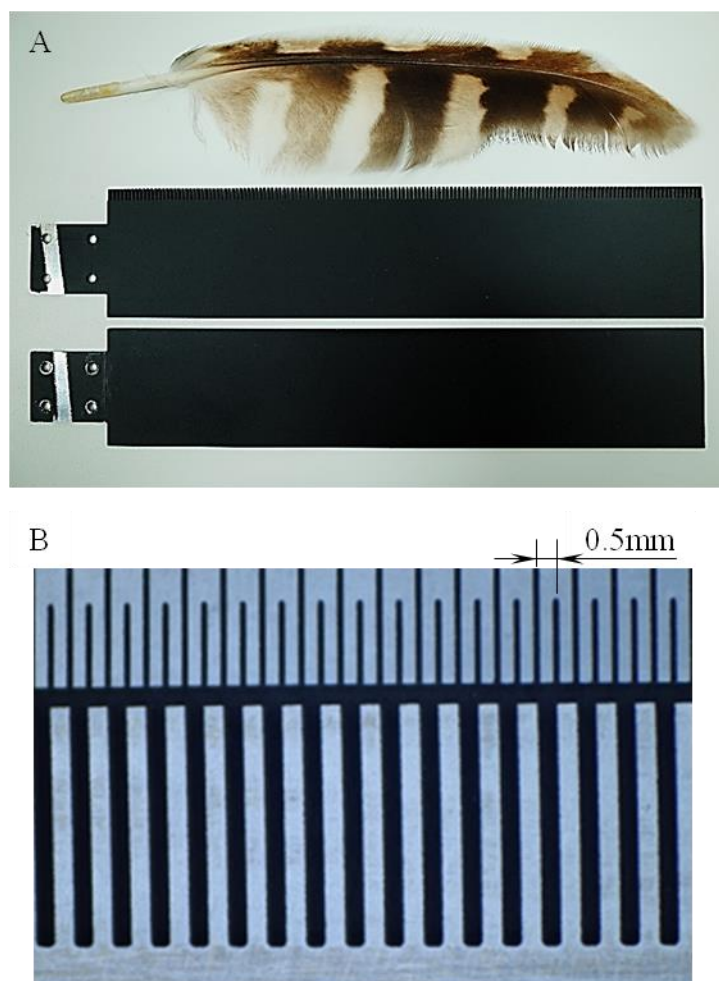
Figure 2-2. (A) Owl single feather (top)-inspired wing models with serrated (middle) and clean (bottom) leading-edges. (B) Close-up view of the leading-edge serrations of the serrated wing model.

2.2 Owl-inspired single-feather wing models with and without leading-edge serrations

Motivated by the serrated leading-edge at the vane of the outermost remex, we fabricated two artificial single-feather wing models (figure 2-2(A)) as 2D rectangular models of leading-edge serrations with different configurations by using a wire electric discharge machine. Note that with a specific focus on the essential aerodynamic effects of comb-like serrations, we here neglected the inclination (bend and twist) angles and the realistic 3D shapes of the serrations. Both models have dimensions of 150×30 mm with an aspect ratio of AR = 5, identical to the outermost remex. For simplicity and tractability, the cross-section is set to be rectangular with a uniform thickness of 0.5 or 1 mm for both models. The serrations-like leading-edge structures of the model are distributed uniformly with a length of 3 mm, matching the real serrations of the owl, approximately 10% of the chord length, with the same spacing and width of 0.5 mm as illustrated in figure 2-2(B).
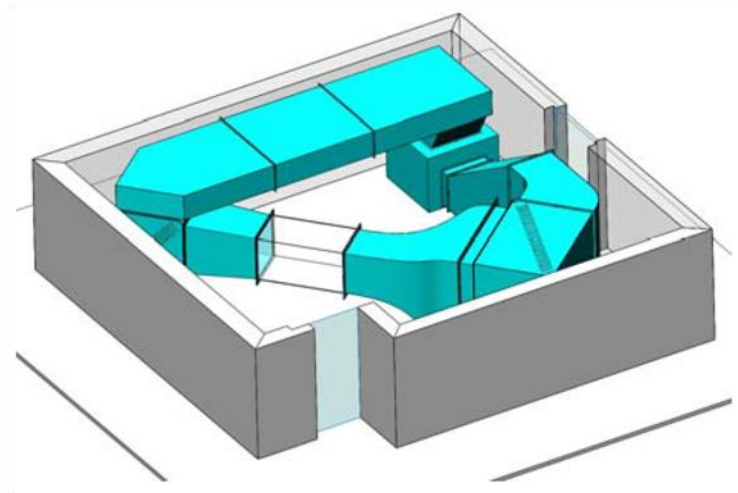
Figure 2-3. Perspective view of an ultra low-speed wind tunnel.

2.3 PIV and force measurements in the low-speed tunnel experiments

Flow fields and aerodynamic characteristics of the single-feather wing model with leading-edge serrations were firstly measured with an ultra low-speed wind tunnel (figure 2-3), which was specifically designed to have a test section of $1 \times 1 \times 2$ m and to be capable for achieving a smooth air-flow ($\leqslant$ 2% turbulence) ranging from 0.5 to 11.0 m/s. The airflow speed was set to be 3.0 m/s, which is within the range of the normal flying speed of owls when attacking prey [1].
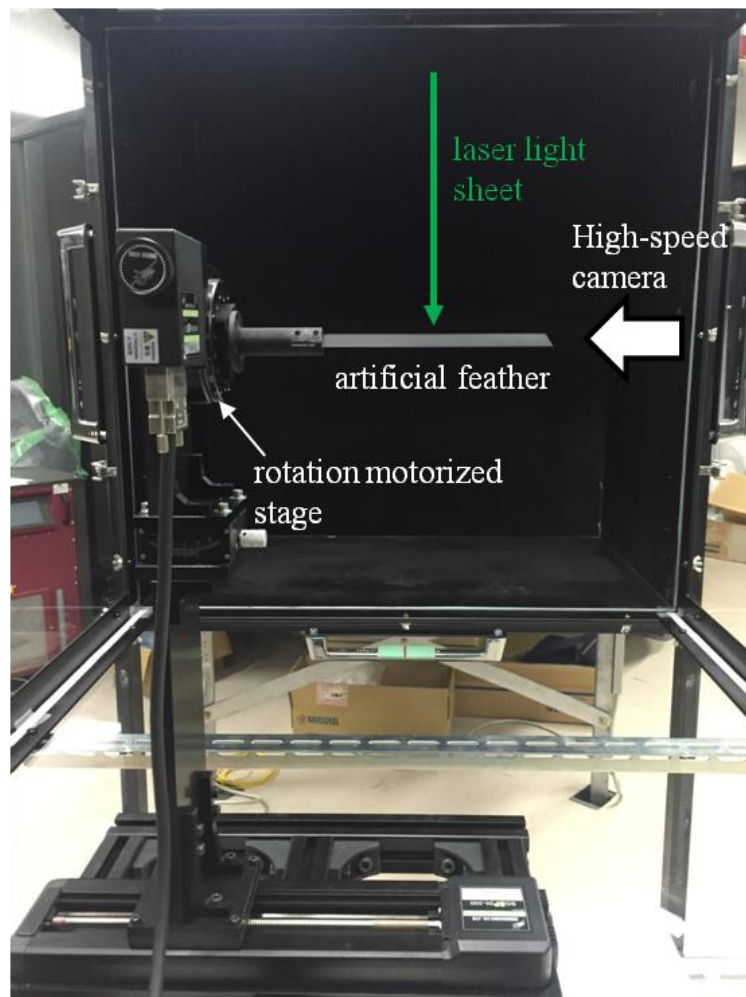
Figure 2-4. Experimental setup for PIV measurements viewing from downstream of the test section.

The single-feather wing models that sit at the center of the test section were put on a rotational motorized stage (SGSP-80YAW, SIGMAKOKI) and attached onto a 6DoF load cell (Nano17Ti, ATI). Time-varying dynamic forces (3000 Hz) acting upon the models were measured and averaged over 10 s to obtain the time-averaged (steady) aerodynamic forces. Near-field flow structures around the models were measured with a PIV system equipped into the low-speed wind tunnel, which was seeded with DEHS mist (1 μm of diameter) generated by a seeding generator (PivPart 14, PivTec). The vertical streamwise plane at mid-wing span was illuminated by a laser light generated by a pulsed laser (532 nm, LDP-100MQG, LeeLaser), which is guided to the top of the test section through optic fiber and then diverged into a 2 mm band sheet through a cylindrical lens with a pulse separation interval of 120 μs. The laser-sheeted area around the wing model (70 × 70 mm) was filmed at 350 Hz by a high-speed camera (FASTCAM SA3, Photron) fitted with a macro lens (150 mm F2.8, SIGMA). The PIV-based filming system was driven by a controller, LC880, LabSmith; and the images were processed by commercial software, Koncerto II, Seika Digital Image. The correlation window was set to have 24 × 24 pixels with 50% overlapped to yield 84 × 84 vectors within one PIV image. The average pixel separation during 120 μs is about 4-5 pixels, with the sub-pixel accuracy of 0.2 pixel according to the manufacturer, which leads to the estimated error of the velocity field between 4-5%. The resulting vectors were further filtered through a threshold to remove the vectors with relatively higher values, which was defined by the standard deviation and the median. The flow velocity field was then calculated by averaging the vectors over 2 s.

More details on this integrated study using PIV and force measurements in wind tunnel experiments on morphology effects of leading-edge serrations can be found in Ikeda et al. [2] The experimental results will also be presented (chapter 4) in comprehensive comparisons with the CFD-based results for validation.

References

[1] Winzen A, Roidl B, Klän S, Klaas and M, Schröder W 2014 Particle-image velocimetry and force measurements of leading-edge serrations on owl-based wing models. *Journal of Bionic Engineering*. **11** 423-438. (http://dx.doi.org/10.1016/S1672-6529(14)60055-X)

[2] Ikeda T, Ueda T, Nakata T, Noda R, Tanaka H, Fujii T and Liu H 2018 Morphology effects of leading-edge serrations on aerodynamic force production: an integrated

24

study using PIV and force measurements. *Journal of Bionic Engineering*. **15** 661-672. (http://doi.org/10.1007/s42235-018-0054-4)

3. Numerical methods

3.1 Overview

In general, since the compressible Navier-Stokes equation describes both the flow and the aeroacoustic fields and thus both may be solved for directly. However, this requires very high numerical resolution due to the large differences in the length scale present between the acoustic variables and the flow variables. On the other hand, it has been widely recognized [1] that the approach splitting the computational domain into two different regions to solve the governing acoustic or flow field with different equations and numerical techniques. This usually involves using two different numerical solvers, first a CFD solver (e.g. direct numerical simulation (DNS), large-eddy simulation (LES), Reynolds-averaged Navier-Stokes equation (RANS)) to solve the flow field and secondly an acoustic solver (e.g. the formula of Lighthill-Curle) to the acoustical propagation.

In this chapter, we first introduce the idealized numerical wing models for CFD modeling, as well as the computational domain and grids (section 3.2). Then, the incompressible LES-based CFD solver for transient flow fields (section 3.3) and acoustic solver for near-field noise spectra (section 3.4) are presented. Note that it is reasonable to assume an incompressible fluid in the LES-based modeling and then use the computed flow fields for the aeroacoustic analysis for a compact computational domain around the wing model [1].

3.2 Computational model of owl-inspired single-feather wing

As illustrated in figure 3-1, based on the owl-inspired experimental models (figure 2-2) we here introduced two idealized single-feather wing models with an infinite wingspan, involving a clean wing model without serrations and a leading-edge-serrated wing model. Note that with consideration of the infinite wingspan, it is reasonable to make CFD modeling of merely one element of the infinite wing and apply transitional periodic boundary conditions on two sides, which leads to a large reduction in computing time. This infinite wing-span model makes it capable to focus on investigating the essential 2D mechanisms associated with leading-edge serrations while neglecting the complexity of 3D effects.

The basic geometric characteristics are summarized in Table 3-1. The coordinate system is defined as in figure 3-1 with its origin at the left side of the leading-edge and located in the middle of the upper and lower surfaces. With consideration of the fact that the force (lift and drag forces) measurements of the artificial single-feather wing models showed little differences associated with the wing thickness [2], here we defined our CFD wing model with a thickness of 0.67 mm in between the range (0.5 ~ 1.0 mm) of the artificial wing models.

Figure 3-1. Computational model of an owl-inspired single-feather wing, with clean (top) and serrated (bottom) leading-edges.
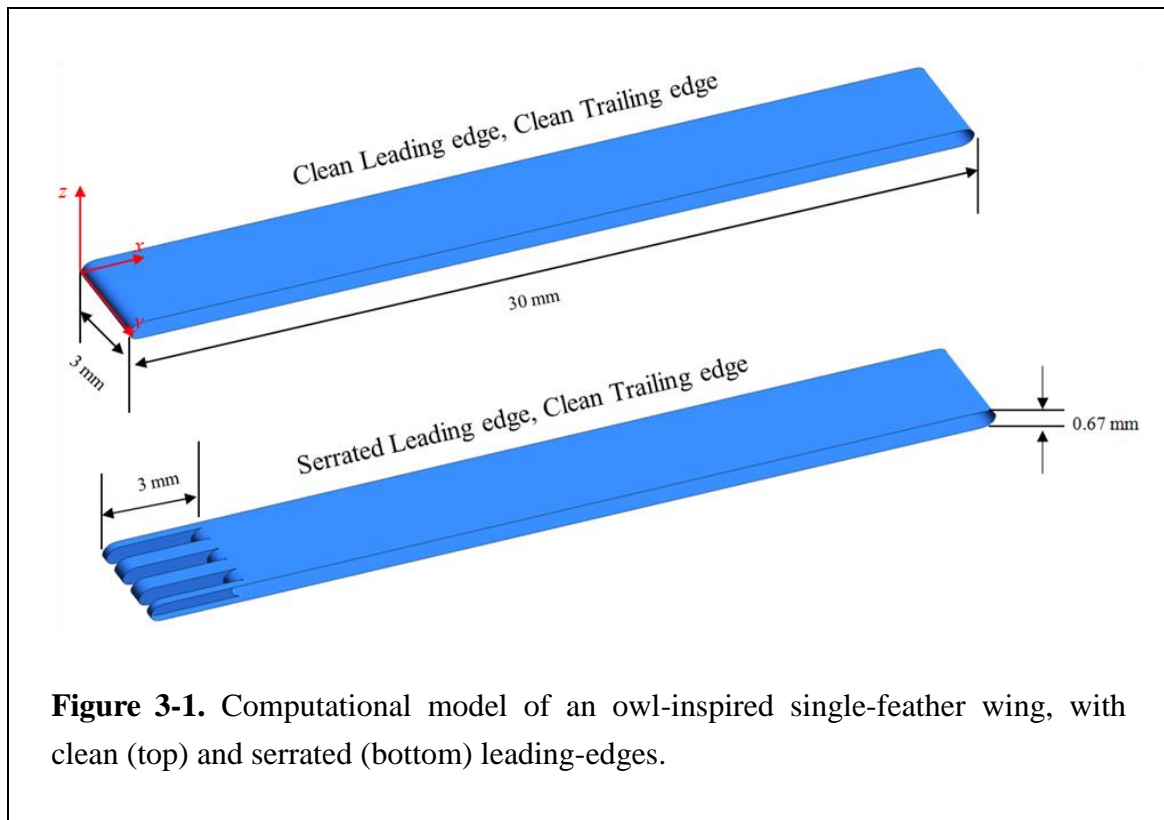
Table 3-1. Basic geometric characteristics of the computational models

Chord length	c	30 mm
Span	b	3 mm
Thickness	s	0.67 mm
Length of serrations	l	3 mm
Width of serrations	w	0.5 mm
Interval between serrations	d	1 mm
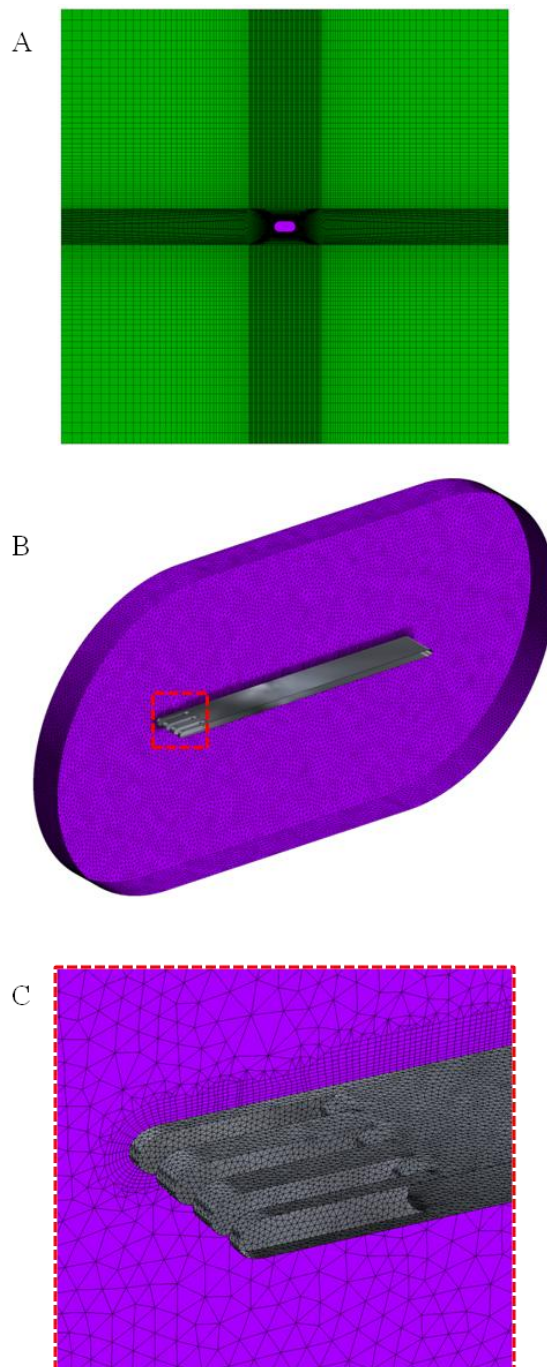
Figure 3-2. Computational domains and grids: (A) H-type structured grids (green) for far-field domain, and (B) "Octree" unstructured grids (purple) for near-field domain. (C) Close-up view of the grids at leading-edge.

To resolve boundary layers and laminar-turbulent transition as well as flow separation around the wing model, a multi-blocked hybrid grid system (figure 3-2) was employed with the near-field domain of $0.5c$ from the wing surface, where c is the chord length. Three unstructured grids with varying mesh densities were generated to perform a mesh sensitivity study (to be discussed in section 4.2). The grids were clustered to the wing surface with the minimum grid spacing adjacent to the surface controlled by a formula [3]

$$\delta_{\min} = \frac{0.1c}{\sqrt{\mathrm{Re}}},$$ (3-1)

where Re is the chord-based Reynolds number. H-type structured grids were generated for the far-field domain with a distance of $20c$ from the wing surface.

3.3 Large-eddy simulation using WALE model

With consideration of the large scale separated flows at a moderate Reynolds number of 6000 (based on inflow velocity $U_{\mathrm{ref}} = 3$ m/s and chord length $c = 3$ cm) in this study, modeling of large-eddy simulation (LES) was adopted, which is capable of resolving laminar-turbulent transition as well as turbulent flow without applying turbulent models rather than RANS (Reynolds-averaged Navier-Stokes equation) modeling. All simulations were herein conducted with commercial software ANSYS CFX (ANSYS, Inc.). Those eddies with smaller scales than the grid size were filtered and involved in a subgrid-scale model in order to reduce computational cost.

For incompressible flows, the filtered governing equations involving the equations of continuity and the momentum can be written such as:

$$\frac{\partial \overline{U_i}}{\partial x_i} = 0,$$ (3-2)

$$\frac{\partial \overline{U_i}}{\partial t} + \frac{\partial}{\partial x_j}\left(\overline{U_i U_j}\right) = -\frac{1}{\rho}\frac{\partial \overline{p}}{\partial x_i} + \frac{\partial}{\partial x_j}\left[\nu\left(\frac{\partial \overline{U_i}}{\partial x_j} + \frac{\partial \overline{U_j}}{\partial x_i}\right)\right] - \frac{\partial \tau_{ij}}{\partial x_j},$$ (3-3)

where the subgrid-scale stress tensor τ_{ij} accounts for the influence of the filtered small scale eddies, and is defined by

$$\tau_{ij} = \overline{U_i U_j} - \overline{U_i}\,\overline{U_j}.$$ (3-4)

Here an eddy-viscosity assumption is used to close the τ_{ij} term, modeled as

28

$$\tau_{ij} - \frac{\delta_{ij}}{3}\tau_{kk} = -2\nu\overline{S}_{ij}, \tag{3-5}$$

where δ_{ij} is the Kronecker symbol, ν_t is the turbulent eddy viscosity, and $\overline{S}_{ij}$ denotes the strain rate tensor of the resolved field defined by

$$\overline{S}_{ij} = \frac{1}{2}\left(\frac{\partial\overline{U}_i}{\partial x_j} + \frac{\partial\overline{U}_j}{\partial x_i}\right). \tag{3-6}$$

We further used the wall-adapted local eddy-viscosity (WALE) model, proposed by Nicoud et al. [4], to compute the eddy viscosity ν_t. The WALE model reads as

$$\nu_t = \left(C_\omega\Delta\right)^2 \frac{\left(S_{ij}^d S_{ij}^d\right)^{\frac{3}{2}}}{\left(\overline{S}_{ij}\overline{S}_{ij}\right)^{\frac{5}{2}} + \left(S_{ij}^d S_{ij}^d\right)^{\frac{5}{4}}}, \tag{3-7}$$

where S_{ij}^d is the traceless symmetric part of the square of the velocity gradient tensor

$$S_{ij}^d = \frac{1}{2}\left(\overline{g}_{ij}^2 + \overline{g}_{ji}^2\right) - \frac{1}{3}\delta_{ij}\overline{g}_{kk}^2, \tag{3-8}$$

where

$$\overline{g}_{ij}^2 = \overline{g}_{ik}\overline{g}_{kj}, \tag{3-9}$$

and

$$\overline{g}_{ij} = \frac{\partial\overline{U}_i}{\partial x_j}, \tag{3-10}$$

denote the velocity gradient tensors. The default value of the constant C_ω is taken to be 0.5. More details on the WALE model can be found in Nicoud et al. [4].

3.4 Calculation of the near-field noise spectrum

With the LES-based transient information of the flow fields we can further conduct an aeroacoustic analysis of the so-called self-noise or near-field noise, which are generally caused by the interaction between a rigid surface and its near-field boundary layer. The calculation of the self-noise spectrum was then done with a post-processing function of CFD-Post (ANSYS, Inc.) through a fast Fourier transform (FFT) algorithm

29

for the time-varying surface pressures. The signal power of the near-field noise spectrum can be calculated in decibel (dB) to give sound amplitude,

$$A_{sp}(f_n) = 10 \cdot \log_{10}\left[\frac{p(f_n)}{p_{\text{ref}}}\right],$$
(3-11)

where $p(f_n)$ denotes the distribution of pressure in the frequency domain, and p_{ref} the reference acoustic pressure, which is equal to 20 μPa.

References

[1] Howe M S 2003 Theory of Vortex Sound (Cambridge: Cambridge University Press)

[2] Ikeda T, Ueda T, Nakata T, Noda R, Tanaka H, Fujii T and Liu H 2018 Morphology effects of leading-edge serrations on aerodynamic force production: an integrated study using PIV and force measurements. *Journal of Bionic Engineering*. **15** 661-672. (http://doi.org/10.1007/s42235-018-0054-4)

[3] Liu H 2009 Integrated modeling of insect flight: from morphology, kinematics to aerodynamics. *Journal of Computational Physics*. **228** 439-459. (http://dx.doi.org/10.1016/ j.jcp.2008.09.020)

[4] Nicoud F and Ducros F 1999 Subgrid-scale stress modeling based on the square of the velocity gradient tensor. *Flow, turbulence and Combustion*. **62** 183-200. (http://dx.doi.org/10.1023/ A:1009995426001)

4. Owl-inspired leading-edge serrations play a crucial role in aerodynamic force production and sound suppression

4.1 Overview

While being a long-standing problem that the unique owl-wing morphologies show apparent association with aerodynamic force production and noise suppression since first reported by Graham [1], it remains unclear how the three morphological characteristics correlate with the aeroacoustic mechanisms. The leading-edge serrations have been the main subject as a sophisticated micro device for passive flow control and aeroacoustic control, which has been widely studied [2-23]. According to the PIV and force measurements on both clean and artificial serrated wing models in a wind tunnel by Klän et al. [23] and Winzen et al. [20], the leading-edge serrations likely provide a tradeoff between aerodynamic force production and noise suppression, and hence play a crucial role in achieving the silent flight of owls. However, the essential underlying mechanisms, such as how the serrated structures influence the flow separations (or instability) and how this affects the force production, still remain uncovered so far. Therefore, aiming at providing a comprehensive understanding of the underlying serration-based aeroacoustic phenomenon, we herein address an integrated study by combining low-speed wind tunnel experiments (introduced in chapter 2) and computational fluid dynamic (CFD) modeling (introduced in chapter 3) with owl-inspired single-feather wing models.

Although the wing motions of free-flying owls generally show complex patterns in wing kinematics and deformations as reported by Wolf et al. [24], as our first step to investigate the essential mechanisms of the leading-edge serrations in steady flow condition, here we pay specific attention to the aerodynamic characteristics of the single-feather models traveling in a uniform incoming flow.

Given the unifrom free-stream velocity $U_{\mathrm{ref}} = 3$ m/s and the chord length $c = 3$ cm, a chord-based Reynolds number was calculated to be Re = 6000. An initial velocity fluctuation was set as $2\% U_{\mathrm{ref}}$, which is identical to the turbulence intensity of the wind

tunnel [25]. A broad range of angles of attack (AoAs) over $0° \leqslant \text{AoA} \leqslant 20°$ was taken into consideration in the CFD modeling based on the measurements by Wolf et al. [24] in which the effective angle of attack was observed to range from -20° to 20° in flapping flights of barn owls. All simulations were performed with a time step of 5×10^{-5} s up to 1 s when the flow fields turned to be stable.

In this chapter, the reliability of our CFD modeling was first verified in section 4.2 in terms of mesh independency, and then further validated in section 4.3 through a comprehensive comparison with PIV and force measurements in wind tunnel [25]. Then, based on the simulated flow structures around clean and serrated models, we give an extensive discussion on how the serrations are capable of passively controlling laminar-turbulent transition and the associated swirling features of leading-edge vortices (section 4.4). Further with an integrated analysis of the simulated velocity spectra, sound spectra, as well as aerodynamic forces, we discuss how the serration-based flows can suppress the vortex shedding-induced instability and hence noise emission, as well as their correlations with lift and drag coefficients, and lift-to-drag ratios (section 4.5).

4.2 Mesh independence study

Here we carried out an extensive verification study of the clean wing model with a specific focus on its self-consistency in terms of mesh independency, which was undertaken at AoA = 5° for steady state with three mesh systems as summarized in Table 4-1.

To evaluate aerodynamic characteristics, e.g. the flow separation and reattachment as well as the laminar-turbulent transition, we calculate pressure and friction coefficients acting upon suction surfaces, which are non-dimensionalized by

$$C_p = \frac{P}{\frac{1}{2}\rho U_{\text{ref}}^2}, \tag{4-1}$$

$$C_f = \frac{\tau_x}{\frac{1}{2}\rho U_{\text{ref}}^2}, \tag{4-2}$$

where P and τ_x denote pressure and streamwise shear stress variations at corresponding node respectively, and ρ is the air density of 1.185 kg/m^3 at 25 °C and 1 atm.
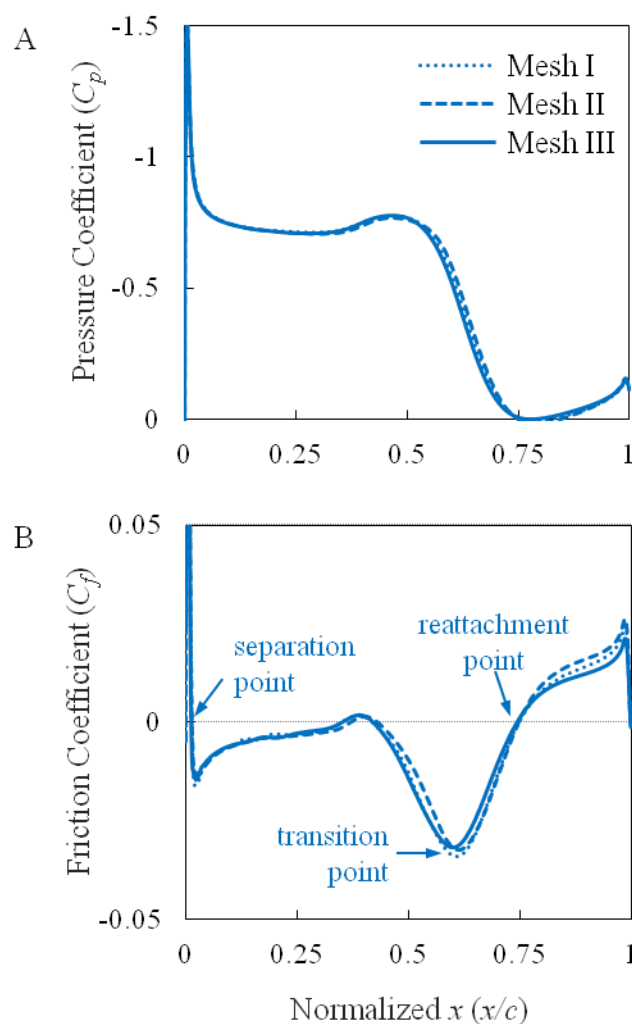
Figure 4-1. Grid independency in terms of time-averaged pressure coefficients (A) and friction coefficients (B) on suction surface of clean leading-edge wing model at AoA = 5° with Mesh I (dotted line), Mesh II (dashed line) and Mesh III (solid line).

Among coarse Mesh I, medium Mesh II, and fine Mesh III with different minimum grid spacing adjacent to the surface and mesh numbers, marginal differences are observed in the distributions of time-averaged pressure coefficient (C_p, see equation 4-1) on the suction surface (figure 4-1(A)). Note that the plateau immediately downstream the suction-pressure peak in the C_p curves indicates a separation bubble and shows seldom discrepancy among the three meshes. Moreover, corresponding with the zero

points and the negative peak of friction coefficient (C_f, see equation 4-2), the separation and reattachment as well as the averaged transition point of the turbulent boundary layer that may be very sensitive to mesh dependency, however, are consistently well predicted with the three meshes (figure 4-1(B)), with a Mesh I-based relative difference by 0.153%c (separation), 1.43%c (transition), 0.47%c (reattachment) as summarized in Table 4-1. The Mesh II could both provide good estimation and save computational time compared with the Mesh III, and therefore was employed for all the other simulations in this study.

Table 4-1. Mesh independency study of clean wing model at AoA = 5° in steady state

	Mesh I	Mesh II	Mesh III
Minimum grid spacing	0.075 mm	0.050 mm	0.025 mm
Node number of the inner domain	308 275	502 622	691 042
Separation point (x/c)	1.206×10^{-2}	1.359×10^{-2}	1.337×10^{-2}
Transition point (x/c)	5.981×10^{-1}	6.124×10^{-1}	6.058×10^{-1}
Reattachment point (x/c)	7.429×10^{-1}	7.464×10^{-1}	7.476×10^{-1}

4.3 Results and validation

4.3.1 Mean velocities

The main flow features around the clean and serrated wing models were visualized by mean velocities in terms of flow separation and reattachment, and compared between the two wing configurations. With ANSYS CFX, it was actually realized by running arithmetic averages of instantaneous velocities, which were statistically generated from the transient velocity fields during LES simulation.

Contours of the time-averaged streamwise velocities normalized by the free-stream velocity are illustrated in figure 4-2 for both serrated and clean wing models at AoAs of 5°, 10°, and 15°, respectively. For comparison and validation of the CFD-based simulations, contours of the PIV-based mean velocity fields measured in wind tunnel experiments are further plotted in figure 4-3 in the same manner, which are in reasonable agreement with the simulated results (to be discussed in section 4.4), and hence validates the reliability of LES-based simulations.

Figure 4-2. Contours of time-averaged velocities normalized by uniform income velocity U_{ref} around a clean leading-edge wing model (left: A, C, E), and a serrated leading-edge wing model (right: B, D, F) at AoAs of 5° (A, B), 10° (C, D), and 15° (E, F), respectively.
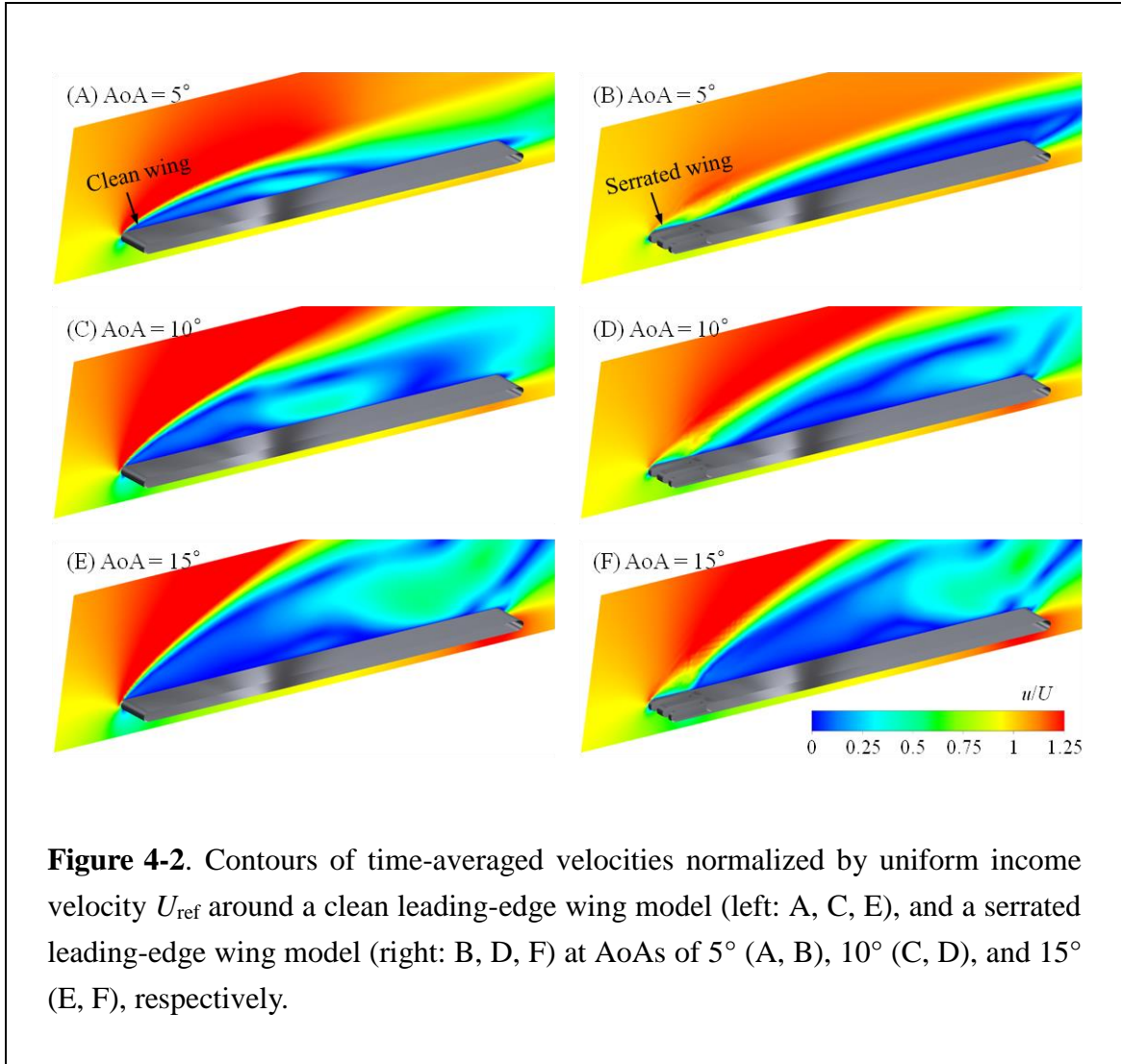
4.3.2 Turbulent fluctuations

To evaluated the turbulent fluctuations in fluid momentum we further plotted the contours of normalized streamwise Reynolds stress R_{uu} (see equations 4-5) in figure 4-4 to visualize the features of laminar-turbulent transition on upper surface. Here the time-averaged Reynolds stress component $\overline{u'v'}$, where u' and v' denote the fluctuation of the corresponding velocity components, is defined as

$$\overline{u'v'} = \overline{uv} - \overline{u}\,\overline{v}, \qquad (4\text{-}3)$$

where the arithmetic averages of the velocity correlation $\overline{uv}$ are statistically generated during the LES computation. The statistical Reynolds stresses can be non-dimensionalized as

35

$$R_{uv} = \frac{\overline{u'v'}}{U_{\text{ref}}^2},$$ (4-4)

whereas the streamwise component is as

$$R_{uu} = \frac{\overline{u'u'}}{U_{\text{ref}}^2}.$$ (4-5)
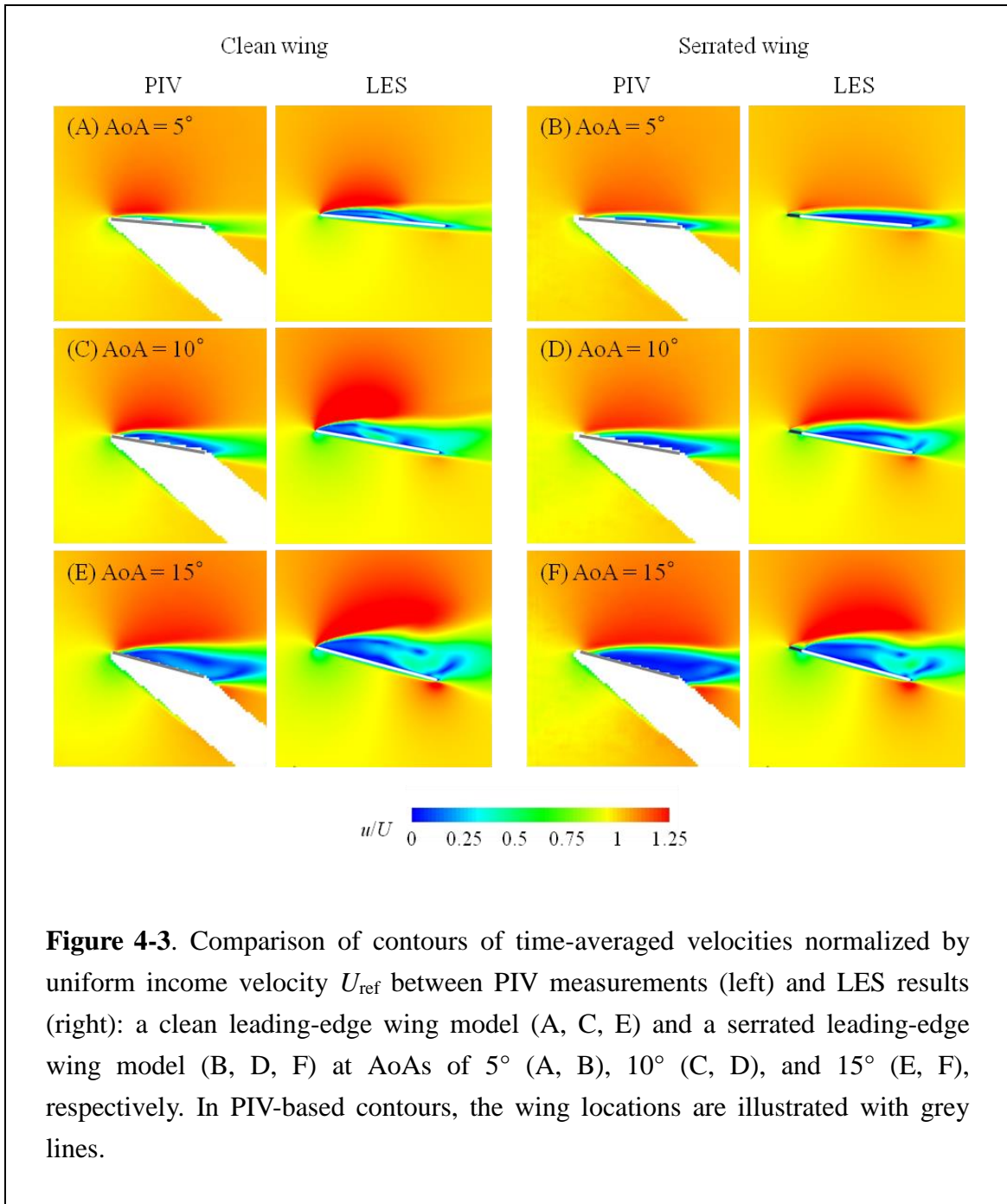
Figure 4-3. Comparison of contours of time-averaged velocities normalized by uniform income velocity U_{ref} between PIV measurements (left) and LES results (right): a clean leading-edge wing model (A, C, E) and a serrated leading-edge wing model (B, D, F) at AoAs of 5° (A, B), 10° (C, D), and 15° (E, F), respectively. In PIV-based contours, the wing locations are illustrated with grey lines.
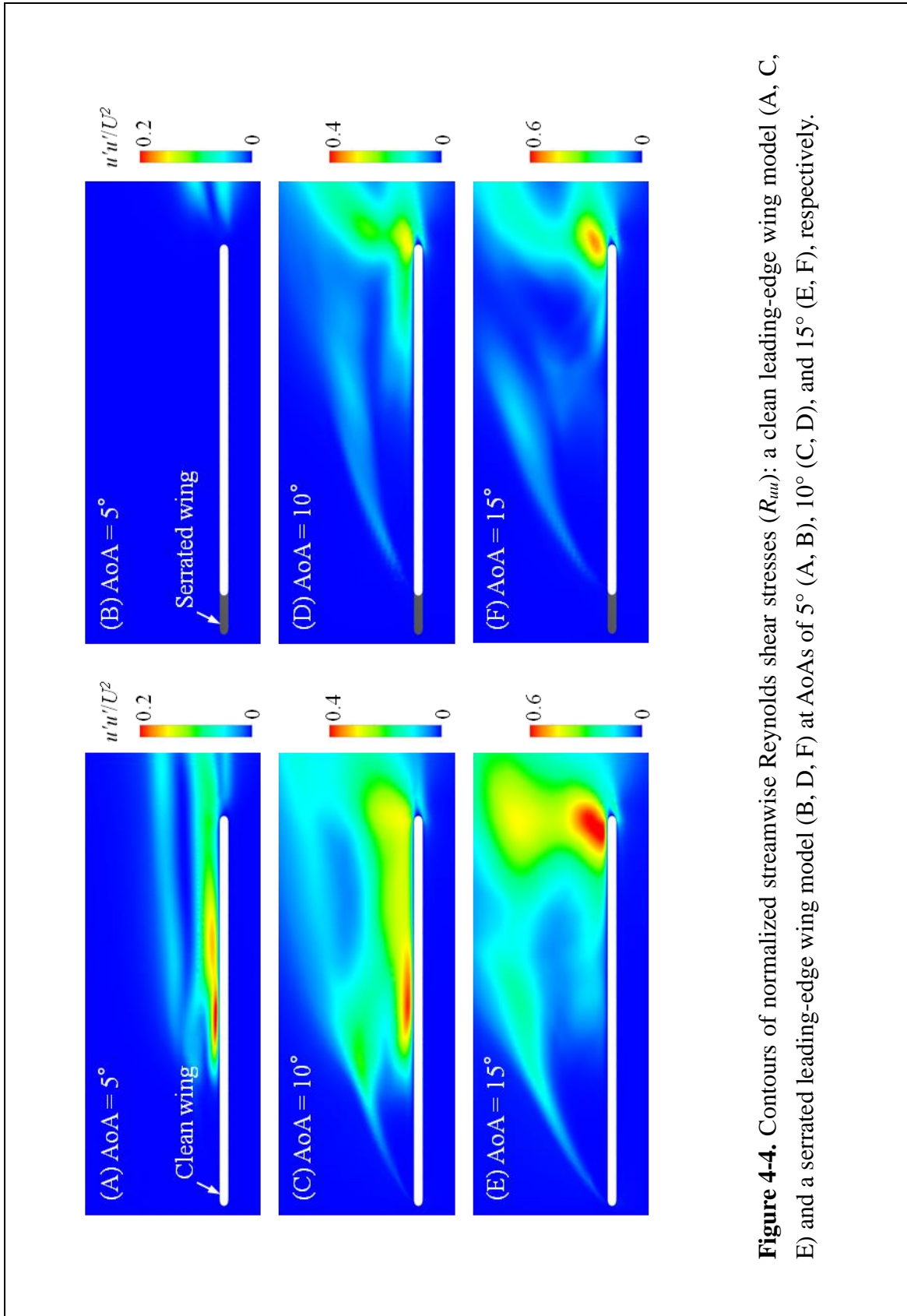
Figure 4-4. Contours of normalized streamwise Reynolds shear stresses (R_{uu}): a clean leading-edge wing model (A, C, E) and a serrated leading-edge wing model (B, D, F) at AoAs of 5° (A, B), 10° (C, D), and 15° (E, F), respectively.
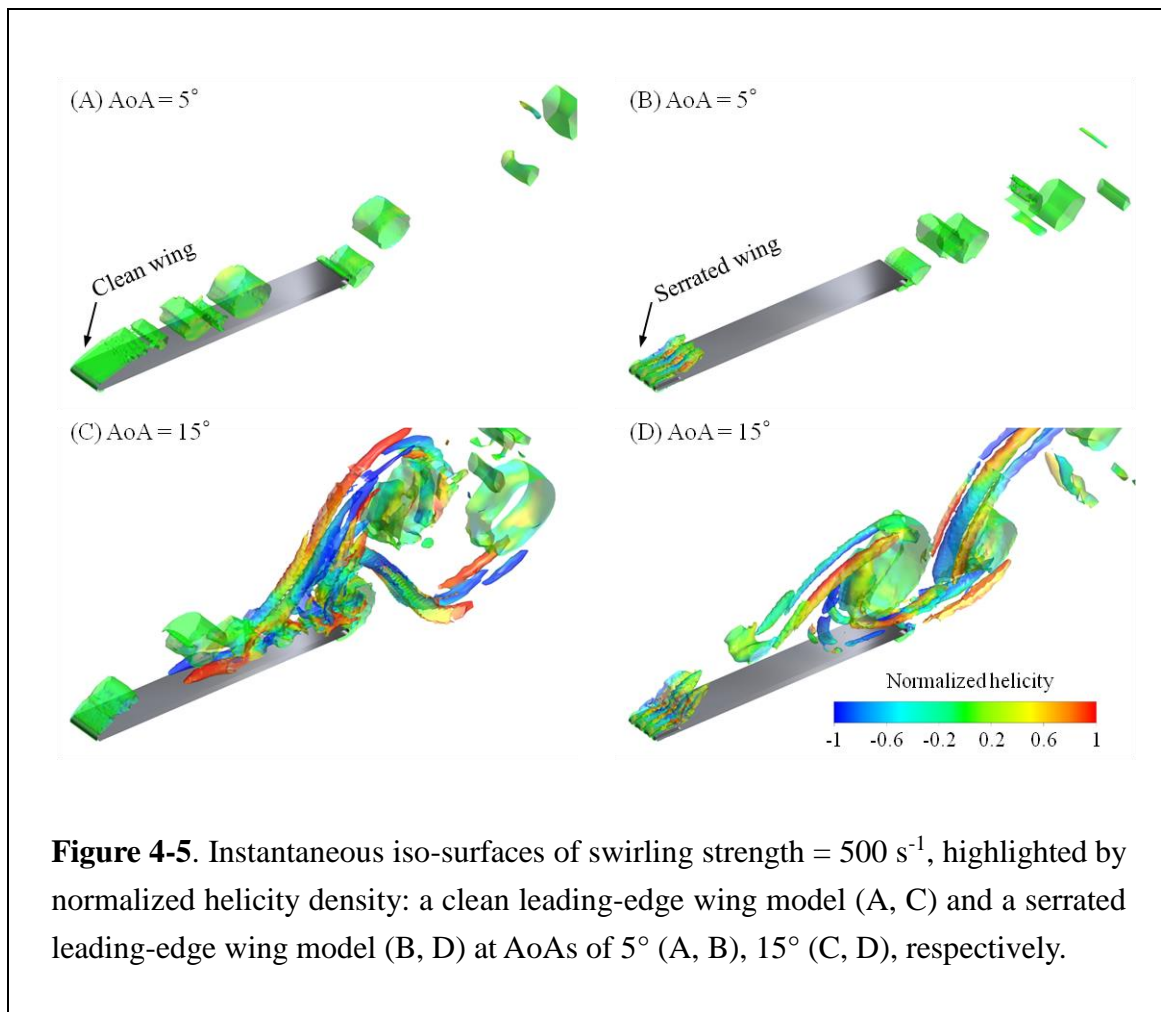
Figure 4-5. Instantaneous iso-surfaces of swirling strength = 500 s^{-1}, highlighted by normalized helicity density: a clean leading-edge wing model (A, C) and a serrated leading-edge wing model (B, D) at AoAs of 5° (A, B), 15° (C, D), respectively.

4.3.3   Vortical structures

Because the laminar-turbulent transition is characterized by vortical structures at leading- and trailing-edge as well as vortex shedding and break-up, we further visualized the instantaneous iso-surfaces of swirling strength that identifies and frames the vortical structure as the region of strengthened vorticity as shown in figure 4-5, with snapshots of the instantaneous iso-surfaces of swirling strength of 500 s^{-1} at AoAs of 5° and 15°. The normalized helicity density [26] is employed simultaneously to visualize the helical feature of the vortical structures, which is defined by

$$h = \frac{U \cdot \omega}{|U| \cdot |\omega|} \, , \tag{4-6}$$

where U and ω denote velocity and vortical vectors, respectively. Note that the

normalized helicity density h is defined as the projection of a fluid's spin vector in the direction of its momentum vector, being positive (red) if it points in the same direction but negative (blue) in the opposite direction.

Figure 4-6. Color balls display the positions of three points at leading-edge (yellow, $x/c = 0$), mid-chord (green, $x/c = 0.5$) and trailing-edge (purple, $x/c = 1$).
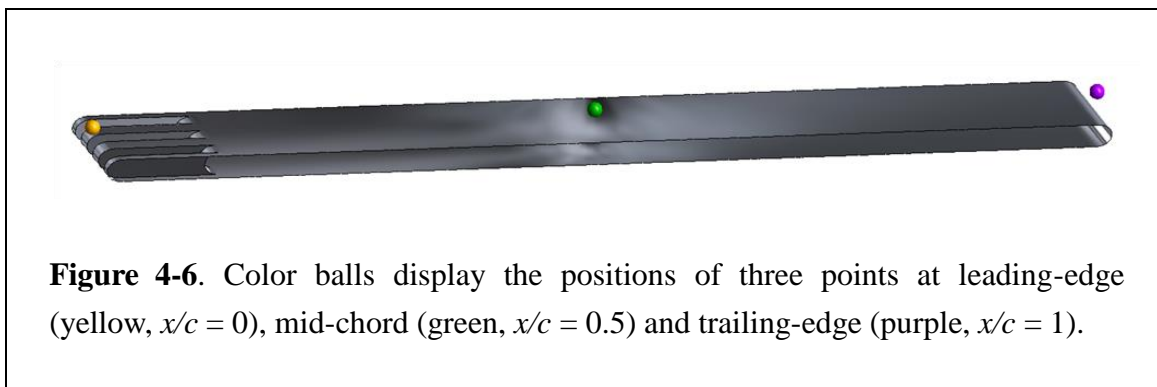
4.3.4   Velocity spectrum

In order to investigate the nature of flow-fluctuation phenomenon during laminar-turbulent transition we further made an analysis and comparison of velocity spectra between the two models at three feature points (as displayed by color balls in figure 4-6) over the upper surface to identify the dominant frequencies of the local velocity fluctuations. The spectrum was obtained via a fast Fourier transform (FFT) algorithm for the time-varying streamwise velocities of the last 4096 time steps. Figure 4-7 illustrates the spectra of streamwise velocities at the leading-edge ($x/c = 0$), the mid-chord ($x/c = 0.5$) and the trailing-edge ($x/c = 1$) and at AoA = 5°, 20°.

4.3.5   Self-noise spectrum

As previously described in section 3.4, with the LES-based transient information of the flow we can further conduct an aeroacoustic analysis of the co-called self-noise or near-field noise, which are generally caused by the interaction between a rigid surface and its near-field boundary layer. The calculation of the self-noise spectrum was then done with a post-processing function of CFD-Post (ANSYS, Inc.) through a FFT of time-varying surface pressures. The signal power of the self-noise spectrum can be calculated in decibel (dB) to give the sound amplitude (see equation 3-11). With the computational time step of 5×10^{-5} s, the upper limit of the spectrum can be calculated up to 20 kHz.
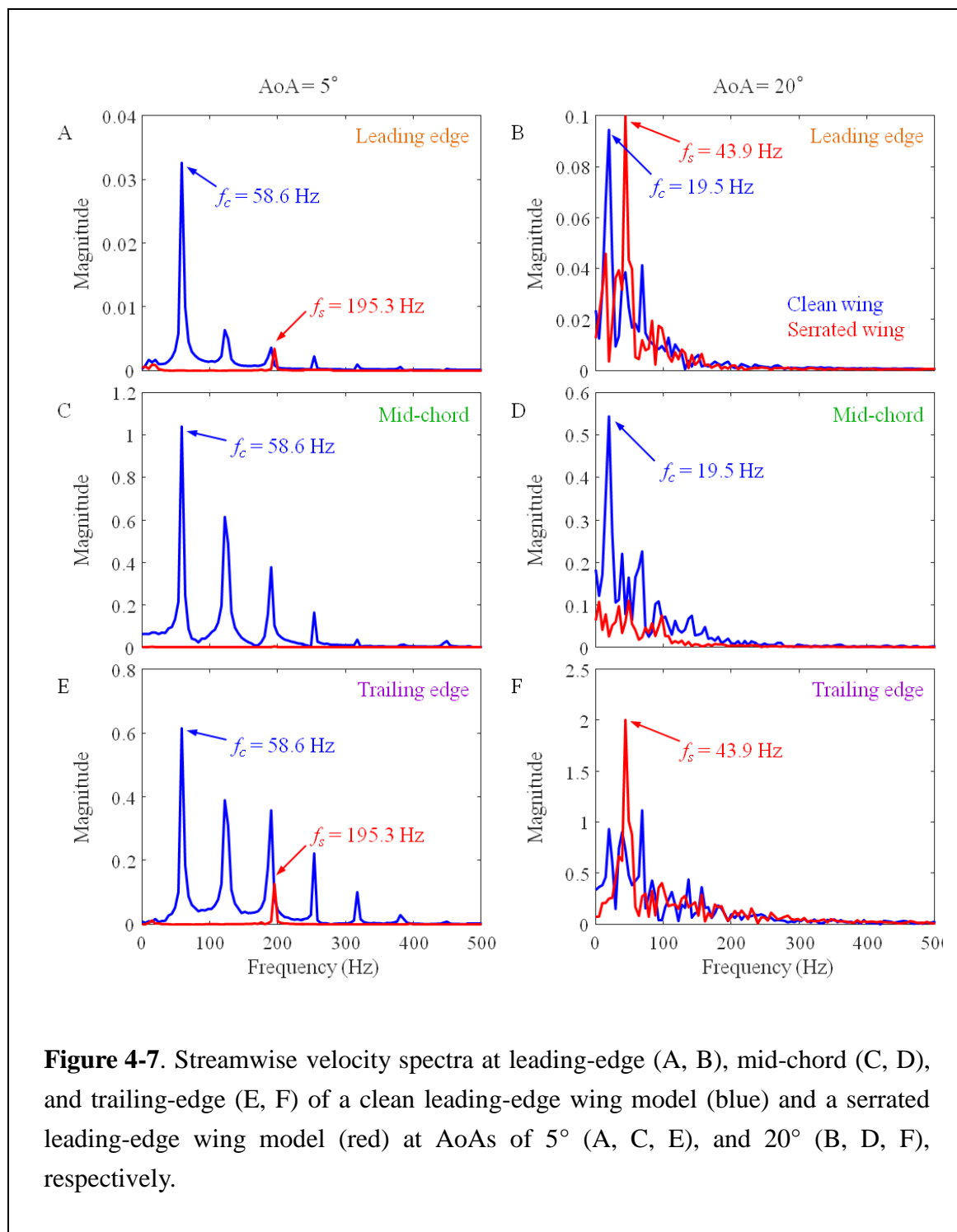
Figure 4-7. Streamwise velocity spectra at leading-edge (A, B), mid-chord (C, D), and trailing-edge (E, F) of a clean leading-edge wing model (blue) and a serrated leading-edge wing model (red) at AoAs of 5° (A, C, E), and 20° (B, D, F), respectively.

As seen in figure 4-4, compared to the leading-edge, distinguished turbulent fluctuations are observed at the trailing-edge. This may lead to a significant increase in the radiated sound power and thus implies that the trailing-edge noise is apparently a

key noise source. To quantify the aerodynamic noise production, we computed the sound amplitude spectra of the trailing-edge self-noise and compared between the clean and serrated wing models at AoA = 20° (figure 4-8), which are identical to an effective angle of attack observed in forward flight of barn owls [24]. Note that the aerodynamic noise is not completely evaluated here because additional noise production may also occur due to flow transition and reattachment, and / or vortex shedding in the separated shear layer and / or in the wake. However, it is obvious that the serrated wing model seems to be capable of remarkably suppressing the level of turbulent fluctuations and hence the noise production at the trailing-edge.
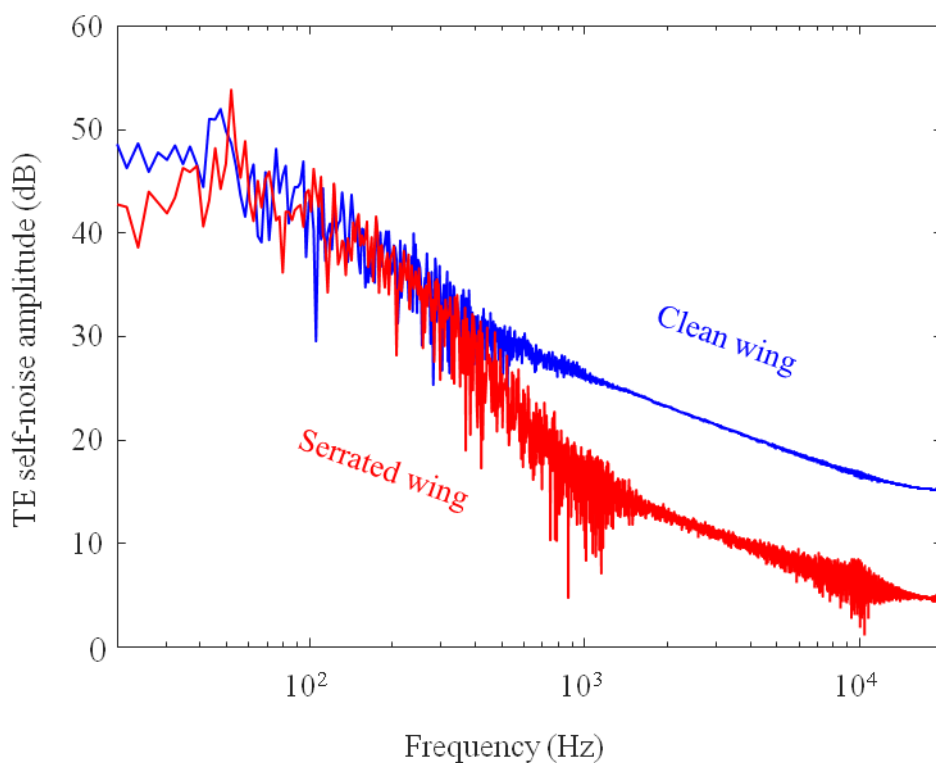
Figure 4-8. Self-noise amplitude spectra at trailing-edge of a clean leading-edge wing model (blue) and a serrated leading-edge wing model (red) at AoA of 20°.
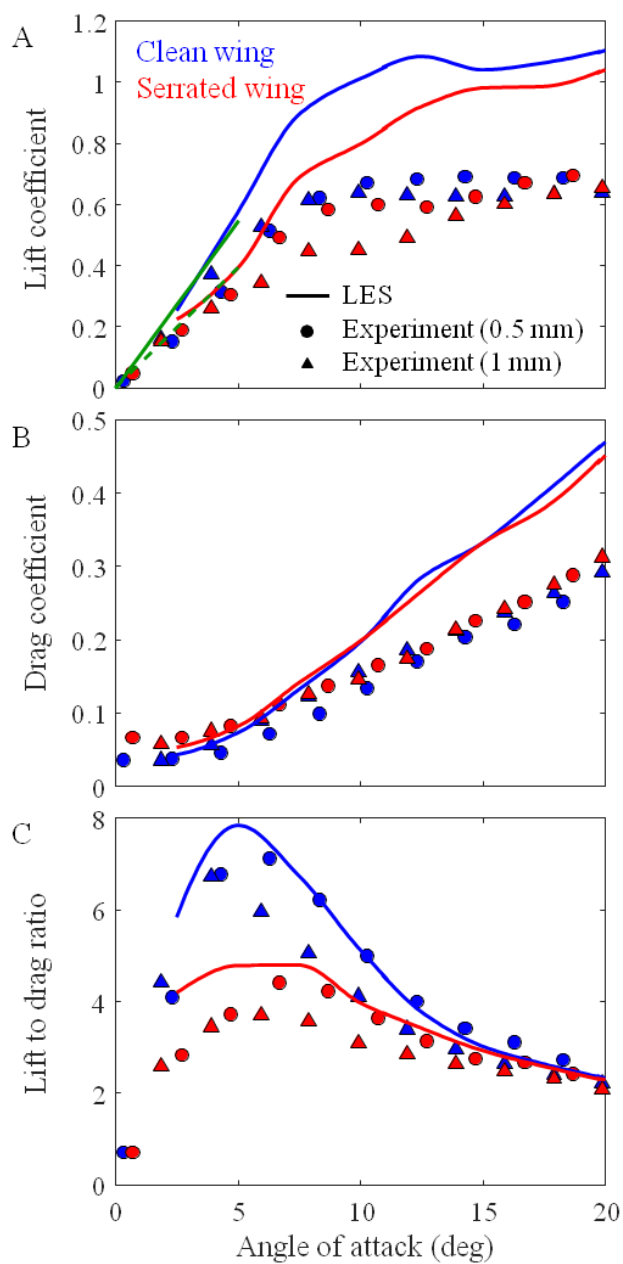
Figure 4-9. Comparison of lift (A) and drag (B) coefficients, and lift-to-drag ratios (C) vs. angles of attack between LES (lines) and wind tunnel experiments (0.5 mm: circles, 1mm: triangles): a clean leading-edge wing model (blue) and a serrated leading-edge wing model (red). Green lines denote lift-curve slopes of a 2D infinite plate (green solid line) and a 3D plate with aspect ratio AR = 5 (green dashed line), respectively, estimated by lifting-line theory.

4.3.6 Aerodynamic forces

As shown in figure 4-9, effects of the leading-edge serrations on aerodynamic performance was further evaluated through a comparison of the time-averaged lift and drag coefficients as well as lift-to-drag ratios via angles of attack between the measurements and simulations. The lift and drag coefficients are defined as follows,

$$C_l = \frac{L}{\frac{1}{2}\rho U_{\text{ref}}^2 S}, \tag{4-7}$$

$$C_d = \frac{D}{\frac{1}{2}\rho U_{\text{ref}}^2 S}, \tag{4-8}$$

where ρ denotes the air density of 1.185 kg/m^3 at 25 °C and 1 atm, and S the wing area of the upper surface that takes into account the area of serrations in the serrated model. It should be noted that the measured aerodynamic force coefficients are for the 3D artificial wing models (see section 2.2) whereas the computed ones are for the 2D infinite wing models without consideration of the 3D effects. In this respect, although we see that the lift-to-drag ratios and the trend of lift and drag coefficients are in very good agreement with each other, there does exist pronounced differences in the magnitudes of lift and drag coefficients in comparison to the EXP models. It should be reasonable to consider that the 3D effect owing to the interplay among the leading-edge vortex, the wing tip vortex and the trailing-edge vortex for the low aspect ratio wing (AR = 5) may largely reduce the aerodynamic force production, in particular at larger angles of attack (figure 4-9).

To further validate our CFD-based results of the 2D wing models, we herein predict the slope of the lift-curve by introducing the thin airfoil theory for 2D flow, which (green solid line) is equal to 2π, agreeing well with our LES-based results (blue solid line) at lower AoAs (figure 4-9). Moreover, the lifting-line theory by Prandtl [27] can be used to quantitatively estimate the lift-curve slope (a) of a 3D plate with medium to large ARs in the following way [28],

$$a = \frac{a_0}{1 + \frac{2}{\text{AR}}}, \tag{4-9}$$

where $a_0 = 2\pi$ is taken to be the lift-curve slope of a 2D infinite plate, and AR = 5 the

aspect ratio of the artificial wing models. Apparently the estimated slope (green dashed line) matches better the measured lift coefficients (blue circles) at low angles of attack. Note that the lifting-line model does not hold for the cases of larger AoAs and stalls.

4.4 Serration-based passive flow control mechanisms

Here, based on the simulated flow structures (mean velocities, turbulent fluctuations and vortical structures) around the clean and serrated wing models, we investigate how the leading-edge serrations passively control the flows during laminar-turbulent transition with a focus on the features of flow separation and reattachment and the associated swirling features of leading-edge vortices, as well as their correlations with the aerodynamic force production of lift and drag.

As shown in figures 4-2 and 4-3, the normalized mean velocity fields demonstrate obvious discrepancy between clean and serrated wing models. An immediate flow separation at the leading-edge is observed in the clean wing model at all AoAs (figures 4-2(A), (C), (E) and 4-3(A), (C), (E)), which is likely owing to the sharp leading-edge and the adverse pressure gradient. The serrated model, however, seems to be capable of filtering the flow via serrations and generates a partial-slip boundary layer in the vicinity of the leading-edge (figures 4-2(B), (D), (F) and 4-3(B), (D), (F)), which obviously delays and mitigates the flow separation downstream. This consequently leads to significantly different flow characteristics on the suction surface.

At a lower AoA of 5°, it is seen that in the clean model (figures 4-2(A) and 4-3(A)) the separated flow reattaches onto the upper surface in the vicinity of approximately x/c = 0.65, forming a separation bubble, i.e. the leading-edge vortex, which supports the results by Winzen et al. [20]. This phenomenon is normally observed in the low Reynolds-number flow regime associated with laminar-turbulent transition on the suction surface [22, 29-30]. The distributions of streamwise Reynolds stress in figure 4-4(A) further demonstrate a laminar flow region at the leading-edge, followed by a rapid transition immediately upstream of the reattachment point as well as an attached turbulent boundary layer. In contrast, the serrated wing model corresponds with a long suction-flow region without reattachment (figures 4-2(B) and 4-3(B)) throughout the upper surface, and shows almost no variations in the streamwise Reynolds stresses associated with the turbulent fluctuations (figure 4-4(B)). This indicates that the suction-flow remains in a completely laminar state owing to the serrations. On the other

hand, due to the lack of the leading-edge vortex, i.e. the leading-edge separation bubble, the serrated wing model obviously shows poor aerodynamic performance in lift (figure 4-9(A)) and drag (figure 4-9(B)) coefficients as well as in lift-to-drag ratio (figure 4-9(C)). This implies that at such a lower angle of attack, the serrated wing seems to pay a cost on stabilizing the flow through delaying the laminar-turbulent transition with a reduction in aerodynamic performance.

Along with increasing of AoA to 10°, it is observed that the leading-edge vortex grows up quickly and it turns out to be difficult to localize the mean reattachment point from the velocity fields (figures 4-2(C), (D) and 4-3(C), (D)). A shear layer is then detected in both clean and serrated wing models at the leading-edge where the flows separate completely from the upper surface as seen in the streamwise Reynolds stresses (figures 4-4(C), (D)). The clean wing model (figure 4-4(C)) shows a complicated phase of laminar-turbulent transition with a shear layer initiated at the leading-edge but growing rapidly over the mid-chord, and substantially developing into fully turbulent at the trailing-edge. The serrated wing model (figure 4-4(D)), however, shows a larger shear layer region with more moderate turbulent fluctuations within it, and the suction-flow remains laminar over most parts of the upper surface, eventually transiting to fully turbulent at the trailing-edge.

Further increase AoA to 15° or beyond leads to enlarging the flow separation, which eventually results in an apparently similar nature of the mean flow fields for the two wing models (figures 4-2(E), (F) and 4-3(E), (F)). The distribution of streamwise Reynolds stress, however, still remains apparently different: the clean wing model (figure 4-4(E)) shows significantly higher instability within the shear layer compared to the serrated wing model (figure 4-4(F)), corresponding to a much larger region of laminar-turbulent transition. Clearly, the turbulent fluctuations in the vicinity of the trailing-edge become much more pronounced with increasing AoAs because of the interplay between the shedding vortices induced by the separated shear layers and the trailing-edge vortices.

To investigate the shear layer-induced flow instability, we further look at the swirling features associated with laminar-turbulent transition. For the clean wing model, it is seen that a free shear layer is formed at the separation point, where the Kelvin-Helmholtz (KH) instability occurs causing oscillations of the separated shear layer, which as shown in figures 4-5(A) and (C) substantially leads to vortex shedding.

45

These shedding vortices dynamically interact with each other and substantially merge together at the mid-chord, which enhances the flow instability, resulting in an intense transition to turbulence. At the lower AoA of 5°, over the mid-chord the turbulent flow entrain momentum to reattach and forms a fully developed turbulent boundary layer downstream (figures 4-2(A) and 4-3(A)) while the shedding vortices flow over the upper surface and shed off from the trailing-edge (figure 4-5(A)). At the higher AoA of 15°, the shedding vortices obviously roll away quickly from the upper surface, growing up to a large-scale vortex sheet in the wake (figure 4-5(C)). In contrast, the serrated wing model shows an obvious different phase: the leading-edge vortex is broken up into numbers of small eddies (figures 4-5(B) and (D)), which likely scatters and mitigates the KH instability within the separated shear layer and hence suppresses the vortex shedding efficiently and consequently leads to enhanced stability of the suction flow.

4.5 Tradeoff between force production and sound suppression

Here we give an extensive discussion on whether serrations may be capable of providing a novel solution to the tradeoff between flow fluctuation-induced noise suppression and force production in owl silent flight. We investigate the dominant frequencies of the flow fluctuations through FFT-based velocity spectrum analysis to clarify how the leading-edge serrations contribute to suppressing the local velocity fluctuations. We further use an FFT-based pressure spectrum analysis to quantify how the discrepancy in the flow fluctuations leads to distinguished sound generation between the clean and serrated wing models.

At a lower AoA of 5°, we see a pronounced difference of velocity spectra between the clean and serrated wing models. The clean model presents a highest peak at $f = 58.6$ Hz at leading-edge (figure 4-7(A)), pointing to the dominant fluctuation frequency of the separated shear layer; and several prominent peaks are also notable at mid-chord and trailing-edge (figures 4-7(C) and (E)), corresponding to high harmonic-frequency eddies in figure 4-5(A), associated with the laminar-turbulent transition (figure 4-4(A)). The serrated wing model, however, obviously shows much lower magnitudes of the dominant fluctuation frequencies throughout the upper surface, merely with a spectral prominence at $f = 195.3$ Hz (figure 4-7(E)) corresponding to the shedding of trailing-edge vortices. This indicates that the leading-edge serrations are capable of suppressing velocity fluctuations to a lower level from leading-edge (figure 4-7(A)) to trailing-edge (figure 4-7(E)), and hence stabilizing the flows due to laminar-turbulent

transition at mid-chord (figure 4-7(C)).

At a larger AoA of 20°, the clean wing model presents a notable increase in the magnitude of flow fluctuations corresponding to the intense laminar-turbulent transition at mid-chord whereas the serrated wing model is obviously capable of suppressing the velocity fluctuations to a lower level (figures 4-7(B) and (D)). At trailing-edge, the clean wing model presents a feature of multiple peaks while one single spectral spike is observed in the serrated wing model at the dominant frequency, $f = 43.9$ Hz (figure 4-7(F)), which is identical to that observed at the leading-edge (figure 4-7(B)). This indicates that the vortices shedding off separately from both leading-edge and trailing-edge likely share the same frequency, which implies that the interactions due to the laminar-turbulent transition at mid-chord have been suppressed remarkably (figure 4-7(D)).

Furthermore, through the FFT-based pressure spectrum analysis, we investigated the sound amplitude spectrum of the trailing-edge self-noise at AoA = 20° (figure 4-8). Obviously, the serrated wing model distinguishably reduces the sound amplitudes by approximately 10 dB in the case when the dominant sound frequency is greater than 2 kHz. This demonstrates that the leading-edge serrations are capable of suppressing high-frequency sound amplitudes at trailing-edge, which are initially induced by the high frequency eddies owing to intense laminar-turbulent transition.

With respect to the force production as illustrated in figure 4-9, the leading-edge serrations demonstrate a distinguished aerodynamic performance between lower and higher angles of attack: reducing the lift coefficient and lift-to-drag ratios at AoAs less than 15° but being capable of achieving an even aerodynamic performance at AoAs greater than 15° compared to the clean wing model. Therefore, with consideration of the tradeoff between aerodynamic force production and sound suppression, it would be fair to say that the serrated wing model pays a cost of lowering aerodynamic performance to achieve sound suppression at lower AoAs < 15° but is capable of resolving the tradeoff to achieve both sound suppression and aerodynamic performance at higher AoAs > 15° where owl wings often reach at in flight [24].

4.6 Summary

In this chapter, we conducted an integrated study by combining LES-based

47

simulations and low-speed wind tunnel experiments on highly unsteady flows associated with laminar-turbulent transition around owl-inspired single-feather wing models with and without leading-edge serrations. We find that the serrated wing model can passively control the laminar-turbulent transition to suppress the high frequency eddies, and hence leads to sound suppression. This mechanism is likely achieved by the leading-edge serrations, which as a flow filter, break up the leading-edge vortex into numbers of small eddies and hence suppress the KH instability within the separated shear layer. With velocity spectrum analysis, we confirm that the leading-edge serrations are capable of stabilizing the flow fluctuations due to laminar-turbulent transition. Further combining with pressure spectrum analysis, we discover that a distinguishable reduction in sound amplitudes of the trailing-edge self-noise can be achieved at a dominant sound frequency greater than 2 kHz. Moreover, the leading-edge serrations seem to be capable of providing a strategy in resolving the tradeoff between noise suppression and force production. We find that, compared to the clean single-feather wing model, the serrated wing model shows a reduction in aerodynamic force production at lower AoAs < 15° but obviously a capability to achieve an even aerodynamic performance at higher AoAs > 15° while significantly suppressing the aeroacoustic noise production. The results further indicate that the owl-inspired leading-edge serrations may provide a useful biomimetic design for flow control and aeroacoustic noise suppression in wind turbines, aircrafts, multi-rotor drones as well as other fluid machinery.

It should be mentioned that the measurements and simulations are all conducted in steady state in order to investigate the essential mechanisms of the leading-edge serrations in gliding flight specifically. It is known that the owls can achieve remarkable maneuvering sophisticatedly while aeroacoustic control even under complex natural turbulent environments. Therefore, the transient conditions will be considered in next chapter to analyze the aerodynamic robustness of the serrated feathers.

Also noted that, for simplicity, in this study we neglected the inclination angles and the realistic 3D shapes of the serrations, as well as the 3D effects induced by wing tip vortices. In addition, other morphological characteristics such as trailing-edge fringes [31-33] and velvety surfaces [22, 29-30] that are not taken into account in this study may also play some role in flow control and aeroacoustic suppression of the serrated wings. Particularly the modifications of the trailing-edge to suppress the aerodynamic noise have been widely studied [34-36]. Furthermore, the flexibility of the natural

feathers leads to fluid-structure interactions during flight. The resulting deformation or aeroelastic flutter of the serrated feather may alter the flow field and the sound production significantly. Therefore, a realistic modeling of owl wings is our next task to unveil how owls utilize an integration of those morphological characteristics complimentarily to achieve silent gliding and flapping flights.

References

[1] Graham RR 1934 The silent flight of owls. *Journal of the Royal Aeronautical Society*. **38** 837-843. (http://dx.doi.org/10.1017/S0368393100109915)

[2] Gruschka HD, Borchers IU and Coble JG 1971 Aerodynamic noise produced by a gliding owl. *Nature*. **233** 409-411. (http://dx.doi.org/10.1038/233409a0)

[3] Kroeger RA, Grushka HD and Helvey TC 1972 Low speed aerodynamics for ultra-quiet flight. *Final Technical Report (July 1970 – May 1971) Tennessee Univ Space Inst Tullahoma* (http://www.dtic.mil/docs/citations/AD0893426)

[4] Lilley GM 1998 A study of the silent flight of the owl. *4th AIAA/CEAS Aeroacoustics Conference, Toulouse, AIAA Paper*. **2340** 1-6. (http://dx.doi.org/10.2514/6.1998-2340)

[5] Chen K, Liu Q, Liao G, Yang Y, Ren L, Yang H and Chen X 2012 The sound suppression characteristics of wing feather of owl (*Bubo bubo*). *Journal of Bionic Engineering*. **9** 192-199. (http://dx.doi.org/10.1016/S1672-6529(11)60109-1)

[6] Wagner H, Weger M, Klaas M and Schröder W 2017 Features of owl wings that promote silent flight. *Interface Focus* **7** 20160078. (http://dx.doi.org/10.1098/rsfs.2016.0078)

[7] Sarradj E, Fritzsche C and Geyer T 2011 Silent owl flight: Bird flyover noise measurements. *AIAA Journal*. **49** 769-779. (http://dx.doi.org/10.2514/1.J050703)

[8] Geyer T, Sarradj E and Fritzsche C 2012 Silent owl flight: Acoustic wind tunnel measurements on prepared wings. *18th AIAA/CEAS Aeroacoustics Conference (33rd AIAA Aeroacoustics Conference), Colorado Springs, AIAA Paper*. **2230** 1-17. (http://dx.doi.org/10.2514/ 6.2012-2230)

[9] Geyer T, Claus VT, Sarradj E and Markus PM 2016 Silent owl flight: The effect of the leading edge comb on the gliding flight noise. *22nd AIAA/CEAS Aeroacoustics Conference, Lyon, AIAA Paper*. **3017** 1-12. (http://dx.doi.org/10.2514/6.2016-3017)

[10] Hersh AS and Hayden RE 1971 Aerodynamic sound radiation from lifting surfaces with and without leading-edge serrations. *NASA-CR-114370*.

[11] Hersh AS, Soderman PT and Hayden RE 1974 Investigation of acoustic effects of leading-edge serrations on airfoils. *Journal of Aircraft*. **11** 197-202. (http://dx.doi.org/10.2514/3.59219)

[12] Arndt REA and Nagel RT 1972 Effect of leading edge serrations on noise radiation from a model rotor. *Society of Naval Architects and Marine Engineers, and U.S. Navy, Advanced Marine Vehicles Meeting, Annapolis, AIAA Paper*. **655**. (http://dx.doi.org/10.2514/6.1972-655)

[13] Soderman PT 1972 Aerodynamic effects of leading-edge serrations on a two-dimensional airfoil. *NASA TECHNICAL MEMORANDUM X-2643*.

[14] Soderman PT 1973 Leading edge serrations which reduce the noise of low-speed rotors. *NASA TECHNICAL NOTE D-7371*.

[15] Collins FG 1981 Boundary-layer control on wings using sound and leading-edge serrations. *AIAA Journal*. **19** 129-130. (http://doi.org/10.2514/3.50930)

[16] Ito S 2009 Aerodynamic influence of leading-edge serrations on an airfoil in a low Reynolds number - A study of an owl wing with leading edge serrations -. *Journal of Biomechanical Science and Engineering*. **4** 117-123. (http://dx.doi.org/10.1299/jbse.4.117)

[17] Narayanan S, Chaitanya P, Haeri S, Joseph P, Kim JW and Polacsek C 2015 Airfoil noise reductions through leading edge serrations. *Physics of Fluids*. **27** 1-17. (http://dx.doi.org/10.1063/1.4907798)

[18] Agrawal BR and Sharma A 2016 Numerical analysis of aerodynamic noise mitigation via leading edge serrations for a rod-airfoil configuration. *International Journal of Aeroacoustics*. **15** 734-756. (http://doi.org/10.1177/1475472X16672322)

[19] Bachmann T, Klän S, Baumgartner W, Klaas M, Schröder W and Wagner H 2007 Morphometric characterisation of wing feathers of the barn owl *Tyto alba pratincola* and the pigeon *Columba livia*. *Frontiers in Zoology*. **4** 1-15. (http://dx.doi.org/10.1186/1742-9994-4-23)

[20] Winzen A, Roidl B, Klän S, Klaas and M, Schröder W 2014 Particle-image velocimetry and force measurements of leading-edge serrations on owl-based wing models. *Journal of Bionic Engineering*. **11** 423-438. (http://dx.doi.org/10.1016/S1672-6529(14)60055-X)

[21] Bachmann T and Wagner H 2011 The three-dimensional shape of serrations at barn owl wings: towards a typical natural serration as a role model for biomimetic applications. *Journal of Anatomy*. **219** 192-202. (http://dx.doi.org/10.1111/j.1469-7580.2011.01384.x)

[22] Klän S, Bachmann T, Klaas M, Wagner H and Schröder W 2009 Experimental analysis of the flow field over a novel owl based airfoil. *Experiments in Fluids*. **46** 975-989. (http://dx.doi.org/10.1007/s00348-008-0600-7)

[23] Klän S, Klaas M and Schröder W 2010 The influence of leading-edge serrations on the flow field of an artificial owl wing. *28th AIAA Applied Aerodynamics Conference, Chicago, AIAA Paper*. **4942** 1-9. (http://dx.doi.org/10.2514/6.2010-4942)

[24] Wolf T and Konrath R 2015 Avian wing geometry and kinematics of a free-flying barn owl in flapping flight. *Experiments in Fluids*. **56**. (http://dx.doi.org/10.1007/s00348-015-1898-6)

[25] Ikeda T, Ueda T, Nakata T, Noda R, Tanaka H, Fujii T and Liu H 2018 Morphology effects of leading-edge serrations on aerodynamic force production: an integrated study using PIV and force measurements. *Journal of Bionic Engineering*. **15** 661-672. (http://doi.org/10.1007/s42235-018-0054-4)

[26] Liu H 2009 Integrated modeling of insect flight: from morphology, kinematics to aerodynamics. *Journal of Computational Physics*. **228** 439-459. (http://dx.doi.org/10.1016/ j.jcp.2008.09.020)

[27] Prandtl L 1920 Theory of lifting surfaces *NACA Technical Note* 9. (https://ntrs.nasa.gov/search.jsp?R=19930080806)

[28] Laitone EV 1989 Lift-curve slope for finite-aspect-ratio wings. *Journal of Aircraft*. **26** 789-790. (http://dx.doi.org/10.2514/3.45841)

[29] Klän S, Burgmann S, Bachmann T, Klaas M, Wagner H and Schröder W 2012 Surface structure and dimensional effects on the aerodynamics of an owl-based wing model. *European Journal of Mechanics - B/Fluids*. **33** 58-73. (http://dx.doi.org/10.1016/j.euromechflu.2011.12.006)

[30] Winzen A, Klaas M and Schröder W 2013 High-speed PIV measurements of the near-wall flow field over hairy surfaces. *Experiments in Fluids*. **54** 1-14. (http://dx.doi.org/10.1007/s00348-013-1472-z)

[31] Jaworski JW and Peake N 2013 Aerodynamic noise from a poroelastic edge with implications for the silent flight of owls. *Journal of Fluid Mechanics*. **723** 456-479. (http://dx.doi.org/ 10.1017/jfm.2013.139)

[32] Jaworski JW and Peake N 2013 Parametric guidance for turbulent noise reduction from poroelastic trailing edges and owls. *19th AIAA/CEAS Aeroacoustics Conference, Berlin, AIAA Paper*. **2007** 1-14. (http://dx.doi.org/10.2514/6.2013-2007)

[33] Clark IA, Alexander WN, Devenport W, Glegg S, Jaworski JW, Daly C and Peake N 2015 Bio-inspired trailing edge noise control. *21st AIAA/CEAS Aeroacoustics Conference, Dallas, AIAA Paper*. **2365** 1-18. (http://dx.doi.org/10.2514/6.2015-2365)

[34] Marsden AL, Wang M, Dennis JE and Moin P 2007 Trailing-edge noise reduction using derivative-free optimization and large-eddy simulation. *Journal of Fluid Mechanics*. **572** 13-36. (http://doi.org/10.1017/S0022112006003235)

[35] Oerlemans S, Fisher M, Maeder T and Kögler K 2009 Reduction of wind turbine noise using optimized airfoils and trailing-edge serrations. *AIAA Journal*. **47** 1470-1481. (http://dx.doi.org/10.2514/1.38888)

[36] Gruber M, Joseph PF and Chong TP 2011 On the mechanisms of serrated airfoil trailing edge noise reduction. *17th AIAA/CEAS Aeroacoustics Conference (32nd AIAA Aeroacoustics Conference), Portland, Oregon, AIAA Paper*. **2781** 1-23. (http://dx.doi.org/10.2514/6.2011-2781)

5. Aerodynamic robustness in owl-inspired leading-edge serrations

5.1 Overview

Owls can achieve silent flight and sophisticated maneuvering while coping with natural turbulent environments [1-9] as shown in figure 5-1. In last chapter, we have demonstrated that the leading-edge serrations can passively control the laminar-turbulent transition over the upper wing surface and hence play a crucial role in aerodynamic force and sound production [10]. However, the simulations [10] and measurements [11] in previous study were all conducted in steady state (i.e. uniform inflow), which means, the mechanisms of the leading-edge serrations were investigated specifically for serrated wings in steady gliding flight. On the other hand, turbulent rejection or aerodynamic robustness associated with leading-edge serrations has almost never been studied yet, according to the best of our knowledge.

Figure 5-1. An owl flies in wind-gust, which may be dealt with two conceptual physical models of wind-gust, (i) a longitudinal fluctuation in inflow; (ii) a lateral fluctuation in wing motion.

Figure 5-2. (A) Computational model of an owl-inspired single-feather wing, with clean and serrated leading-edges in ideal wind-gust conditions with (B) a sinusoidal fluctuated free-stream velocity and (C) a sinusoidal fluctuated pitch angle.

Here, follow our previous study in last chapter, we further address a large-eddy simulation (LES)-based study of aerodynamic robustness in owl-inspired leading-edge serrations on two idealized owl-inspired single-feather wing models with infinite wingspan (figure 5-2(A)). The LES modeling of the two computational models in steady state (i.e. uniform free-stream velocity U_{ref} = 3 m/s, chord-based Re = 6000) is used as a baseline to investigate the aerodynamic robustness. An initial velocity fluctuation was set as 2%U_{ref}, a broad range of AoAs over $0° \leqslant \Phi \leqslant 20°$ was considered, a time step of 5×10^{-5} s was specified and all simulations were performed up to 1 s when the flow fields were confirmed to become stable as presented in last chapter.

Then we propose two conceptual physical models (section 5.2) to mimic the wind-gusts under a longitudinal fluctuation in free-stream inflow (figure 5-1(i)) and a lateral fluctuation in pitch angle (figure 5-1(ii)) acting on the two models with and without leading-edge serrations over $0° \leqslant \Phi \leqslant 20°$. The computed flow structures in terms of streamwise Reynolds stress (section 5.3.1), velocity spectra (section 5.3.2) as well as lift and drag coefficients and lift-to-drag ratios (section 5.3.3) are described compared with the baseline cases respectively. We further give an extensive discussion on the aerodynamic robustness associated with the capability of the leading-edge serrations in passively controlling laminar-turbulent transitions as well as their correlations with lift and drag coefficients, and lift-to-drag ratios under fluctuated inflow (section 5.4) and fluctuated wing motion (section 5.5).

5.2 Two conceptual wind-gust models

As illustrated in figure 5-1, we assume that the wind-gust can be modeled in two manners: (i) a horizontal fluctuation in inflow; and (ii) a vertical fluctuation in wing motion. Here realistic turbulence environments in terms of the flow variability or gustiness are represented ideally by introducing the fluctuations in horizontal and vertical direction, which is linked to the aerodynamic force production and hence power requirements of flight [12].

Then the wind-gust disturbance acting on the computational models with and without leading-edge serrations was implemented with two proposed conceptual physical models as illustrated in figure 5-2(A): a periodic longitudinal fluctuation in free-stream velocity as a gust disturbance in horizontal direction, and a periodic lateral fluctuation in pitch angle as a gust disturbance in vertical direction. As shown in figures 5-2(B) and (C), the wing model is either exposed to a horizontal disturbance with a fluctuated inflow or a vertical disturbance with a fluctuated wing pitch after a sufficient period of steady state, which are defined with a sinusoidal function, such as:

$$U_{\text{inflow}}(t) = U_{\text{ref}} + u \cdot \sin(2\pi ft), \tag{5-1}$$

$$\Phi(t) = \Phi + \alpha \cdot \sin(2\pi ft), \tag{5-2}$$

where the fluctuations in inflow and pitch angle were taken to be $u = 0.10U_{\text{ref}}$, $0.25U_{\text{ref}}$, and $\alpha = 1°$, $2°$, respectively. The fluctuation frequency was set to be $f = 5$ Hz, which is identical to the measured flapping frequency of a free-flying barn owl [13].

Here with consideration of that sustained turbulence or gusts can influence aerodynamic performance as well as flight costs when the turbulent components are of similar scales to the animals themselves because kinematic or aerodynamic adjustments will be required to maintain flight stability [14]. Thus the wind-gust models are highly idealized and conceptual but the time scale, i.e. the period and the amplitude of the fluctuations are reasonable sufficiently to mimic the physical situations of the realistic wind-gusts in owl gliding and / or flapping flights.

5.3 Results

5.3.1 Unsteadiness in Reynolds stress

To quantify and compare the aerodynamic unsteadiness in clean and serrated wing models undergoing gust disturbances, turbulent fluctuations in fluid momentum and mean flow fluctuations were first visualized in terms of Reynolds stress. For the case of longitudinal fluctuation in inflow with periodic gust disturbance, contours of streamwise component of the Reynolds stress tensor (R_{uu}, see equation 4-5) were depicted in figures 5-3, 5-4, 5-5 and 5-6 to illustrate the features of laminar-turbulent transition on upper surface for both clean and serrated wing models at $\Phi = 5°$, $10°$, $15°$ and $20°$, respectively. Similarly for the case of lateral fluctuation in pitch angle with periodic gust disturbance, we plotted the contours of streamwise Reynolds stress of the two models in figures 5-11, 5-12, 5-13 and 5-14 at $\Phi_0 = 5°$, $10°$, $15°$ and $20°$, respectively.

5.3.2 Unsteadiness in velocity spectrum

We further visualized and made a comparison of velocity spectrum between the two wing models at three feature points (displayed by color balls in figure 4-6) over the upper surface to investigate the unsteadiness nature of flow-fluctuation phenomenon in gust disturbance through analyzing the dominant frequencies of the local velocity fluctuations. The velocity spectra were calculated with a fast Fourier transform (FFT) algorithm for the time-varying streamwise velocities as previously introduced in last chapter. Figures 5-7 and 5-8 show the spectra of streamwise velocities for both clean and serrated models in inflow fluctuation at $\Phi = 5°$, $15°$ whereas figures 5-15 and 5-16 are in pitching fluctuation at $\Phi_0 = 5°$, $15°$, respectively.
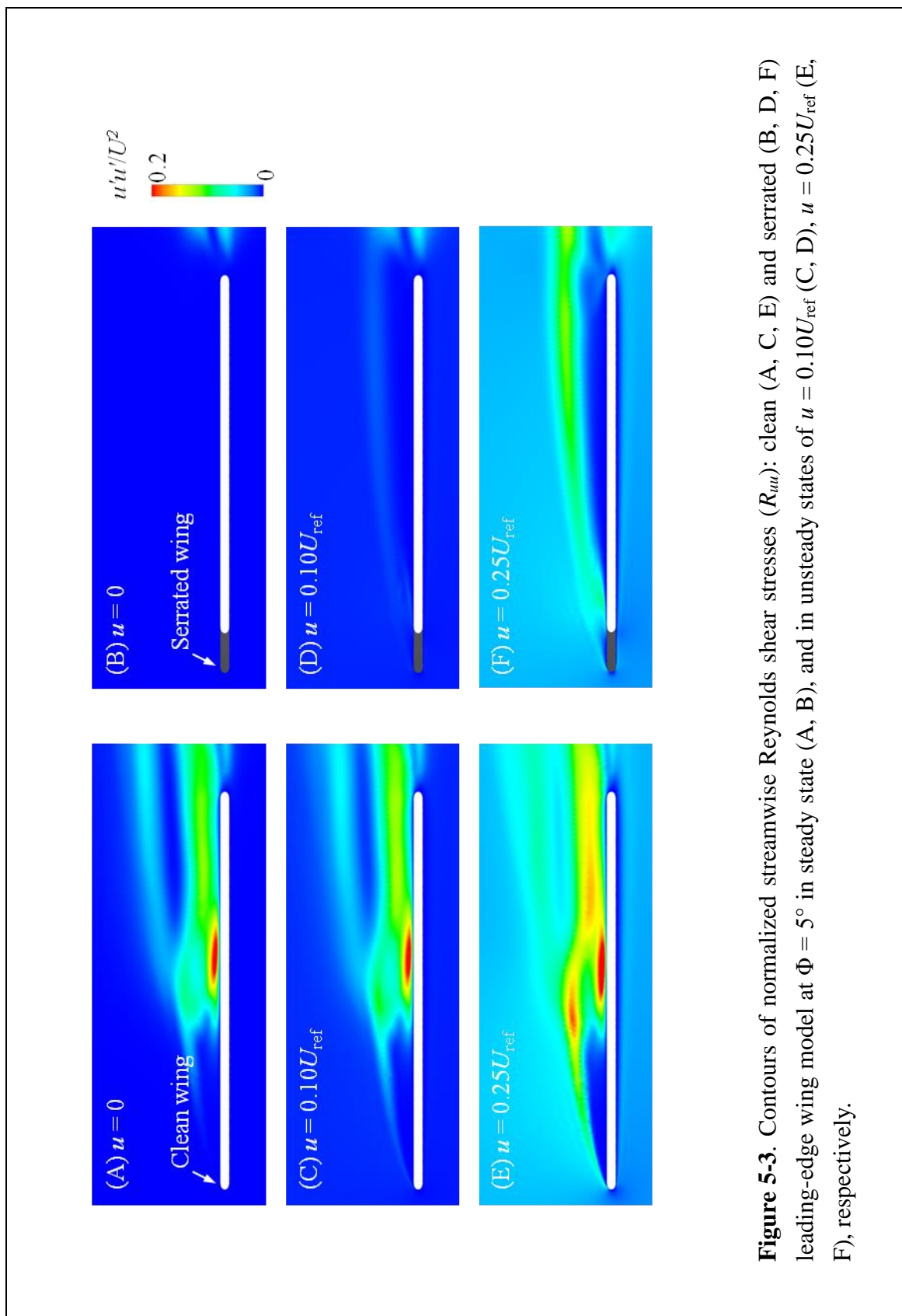
Figure 5-3. Contours of normalized streamwise Reynolds shear stresses (R_{uu}): clean (A, C, E) and serrated (B, D, F) leading-edge wing model at $\Phi = 5°$ in steady state (A, B), and in unsteady states of $u = 0.10U_{ref}$ (C, D), $u = 0.25U_{ref}$ (E, F), respectively.
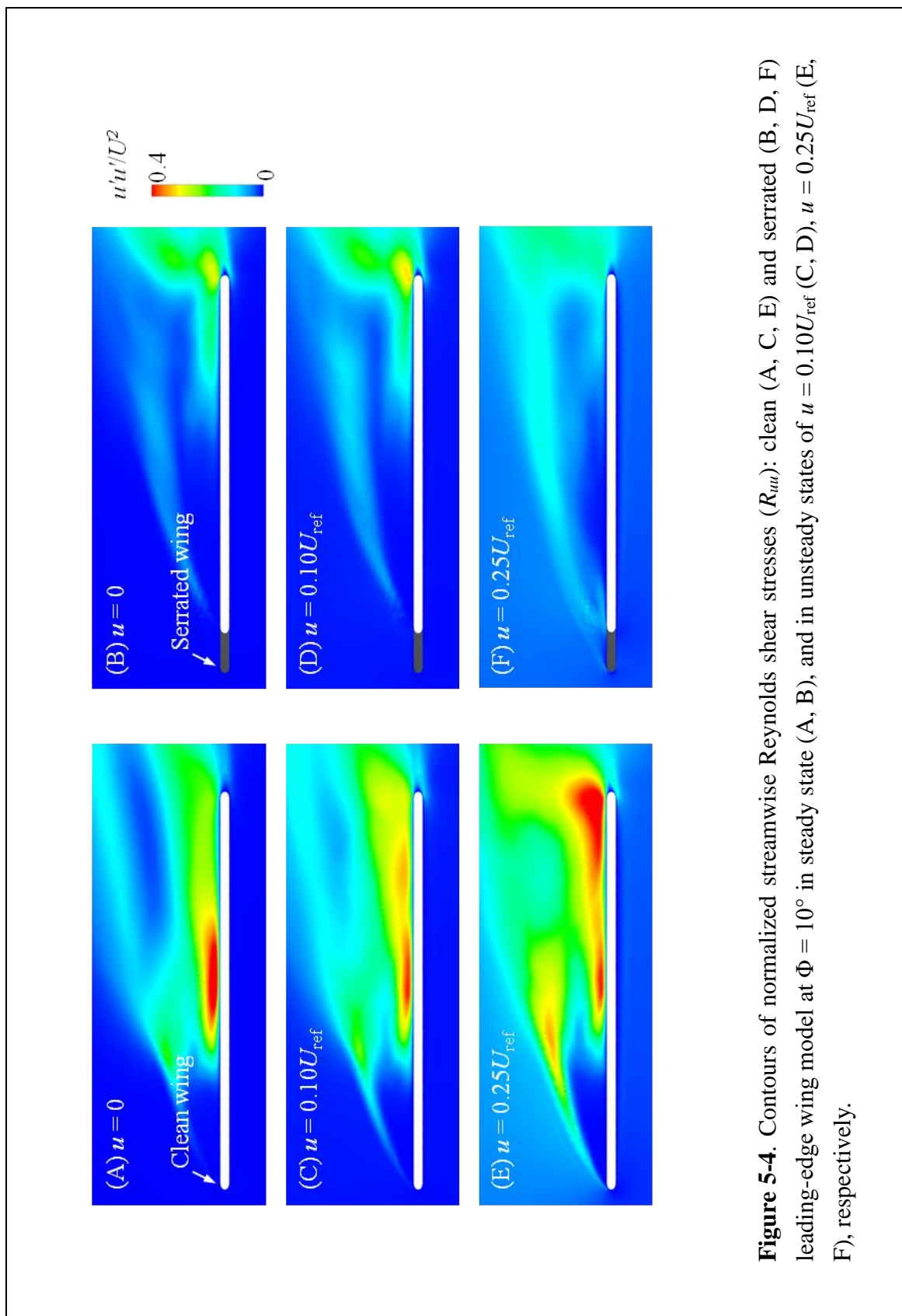
Figure 5-4. Contours of normalized streamwise Reynolds shear stresses (R_{uu}): clean (A, C, E) and serrated (B, D, F) leading-edge wing model at $\Phi = 10°$ in steady state (A, B), and in unsteady states of $u = 0.10U_{ref}$ (C, D), $u = 0.25U_{ref}$ (E, F), respectively.
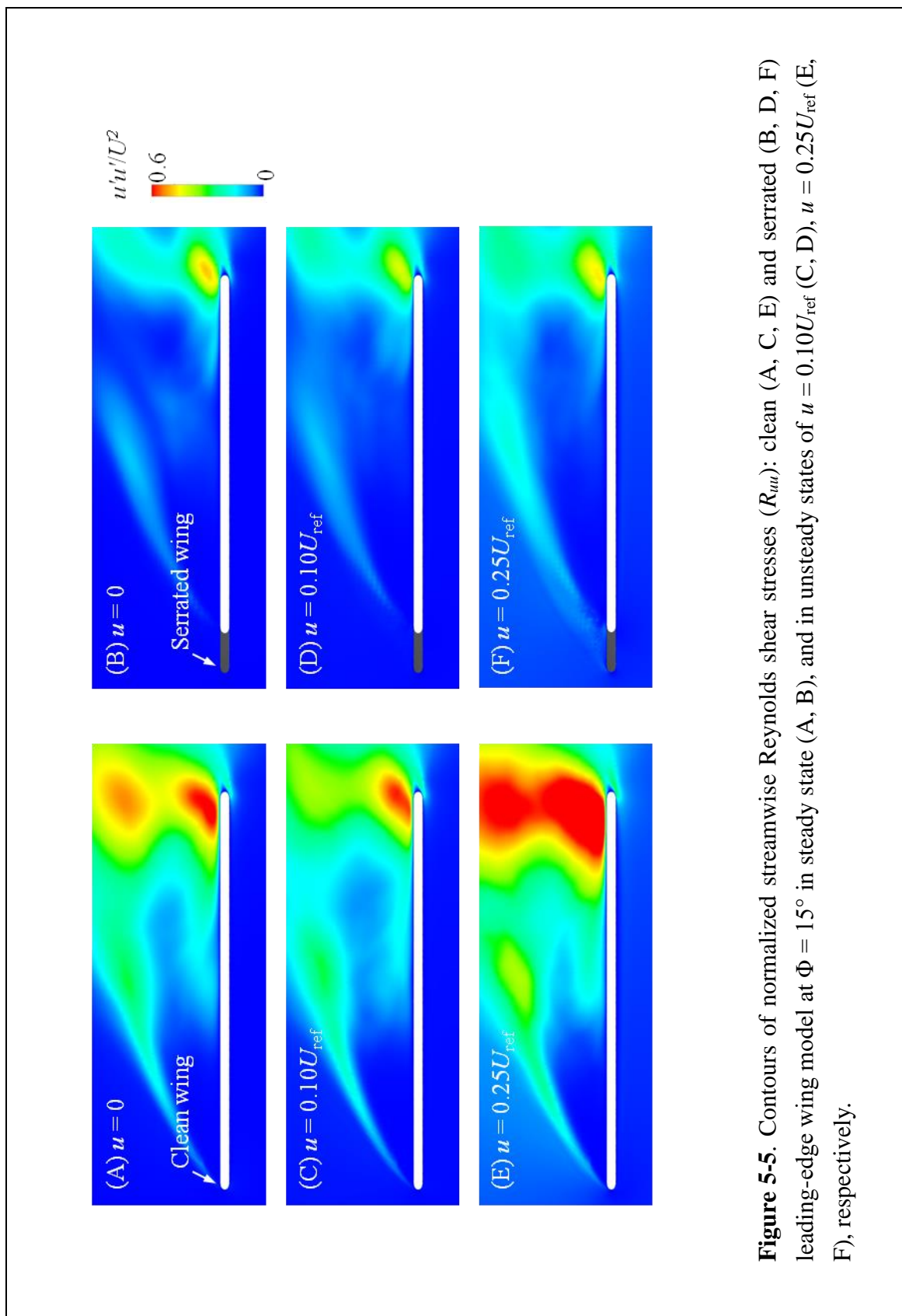
Figure 5-5. Contours of normalized streamwise Reynolds shear stresses (R_{uu}): clean (A, C, E) and serrated (B, D, F) leading-edge wing model at $\Phi = 15°$ in steady state (A, B), and in unsteady states of $u = 0.10U_{\text{ref}}$ (C, D), $u = 0.25U_{\text{ref}}$ (E, F), respectively.

Figure 5-6. Contours of normalized streamwise Reynolds shear stresses (R_{uu}): clean (A, C, E) and serrated (B, D, F) leading-edge wing model at $\Phi = 20°$ in steady state (A, B), and in unsteady states of $u = 0.10U_{ref}$ (C, D), $u = 0.25U_{ref}$ (E, F), respectively.
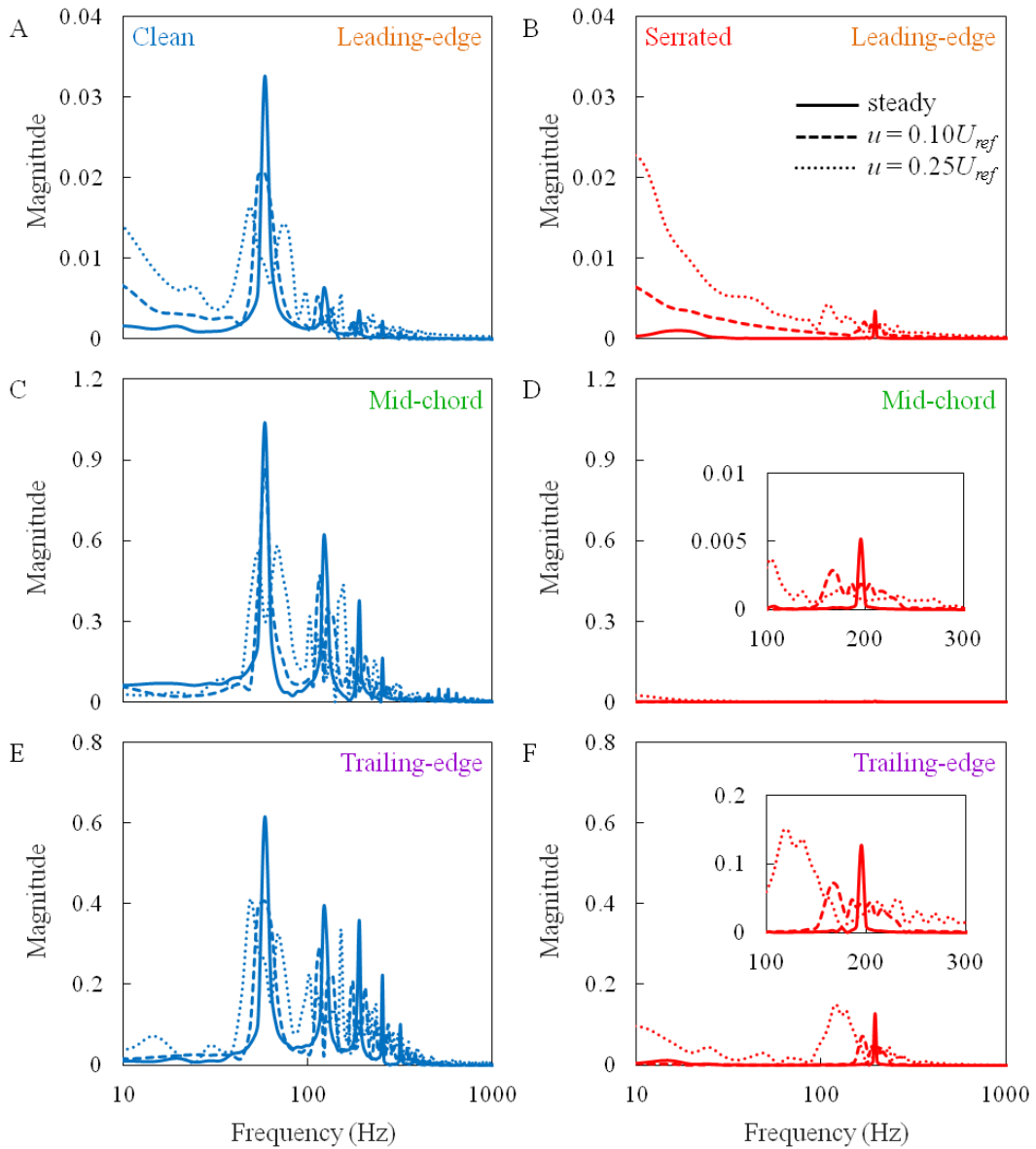
Figure 5-7. Streamwise velocity spectra at leading-edge (A, B), mid-chord (C, D), and trailing-edge (E, F) of clean (blue) and serrated (red) leading-edge wing models at $\Phi = 5°$ in steady state (solid line) and with $u = 0.10U_{ref}$ (dashed line) and $u = 0.25U_{ref}$ (dotted line) in unsteady state, respectively.
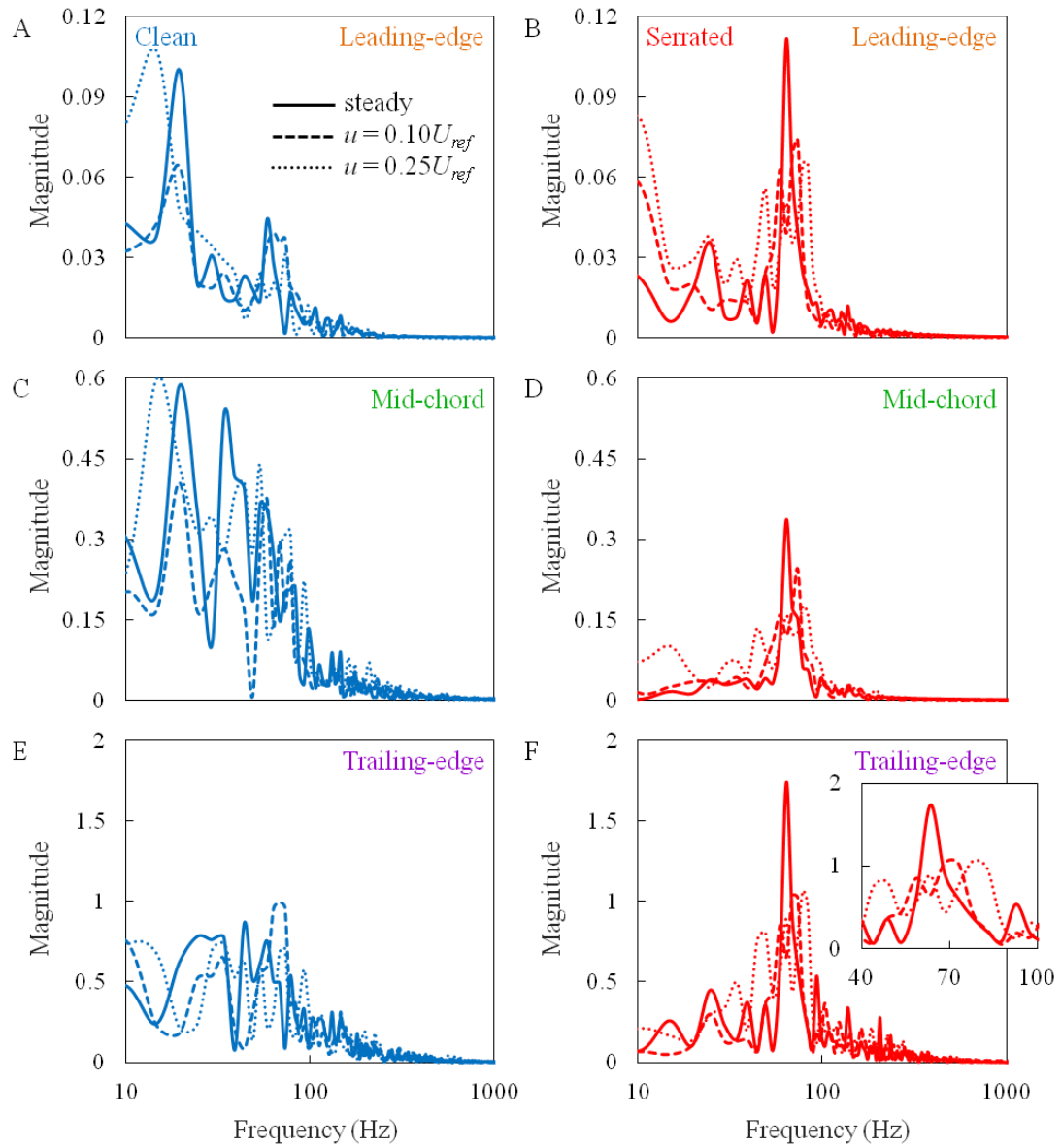
Figure 5-8. Streamwise velocity spectra at leading-edge (A, B), mid-chord (C, D), and trailing-edge (E, F) of clean (blue) and serrated (red) leading-edge wing models at $\Phi = 15°$ in steady state (solid line) and with $u = 0.10U_{\text{ref}}$ (dashed line) and $u = 0.25U_{\text{ref}}$ (dotted line) in unsteady state, respectively.
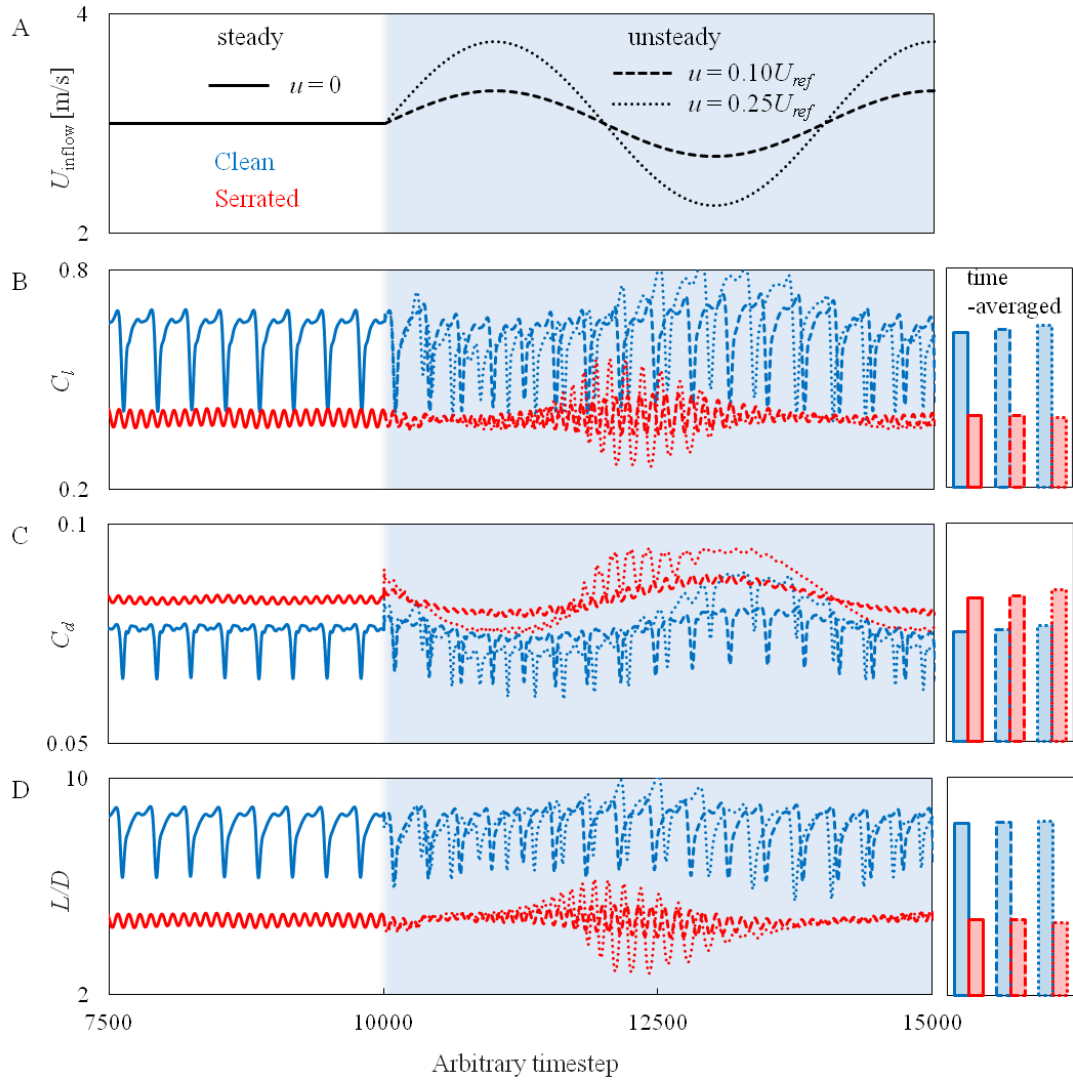
Figure 5-9. Transient characteristics in inflow disturbance. (A) Time-varying free-stream velocities with steady ($u = 0$) and unsteady ($u = 0.10$, $0.25U_{ref}$) phases, time courses of lift (B) and drag (C) coefficients, as well as lift-to-drag ratios (D) associated with clean (blue) and serrated (red) leading-edge wing models at $\Phi = 5°$ in steady (solid lines) and unsteady (dashed, dotted lines) state, respectively.

Figure 5-10. Transient characteristics in inflow disturbance. (A) Time-varying free-stream velocities with steady ($u = 0$) and unsteady ($u = 0.10, 0.25U_{ref}$) phases, time courses of lift (B) and drag (C) coefficients, as well as lift-to-drag ratios (D) associated with clean (blue) and serrated (red) leading-edge wing models at $\Phi = 15°$ in steady (solid lines) and unsteady (dashed, dotted lines) state, respectively.
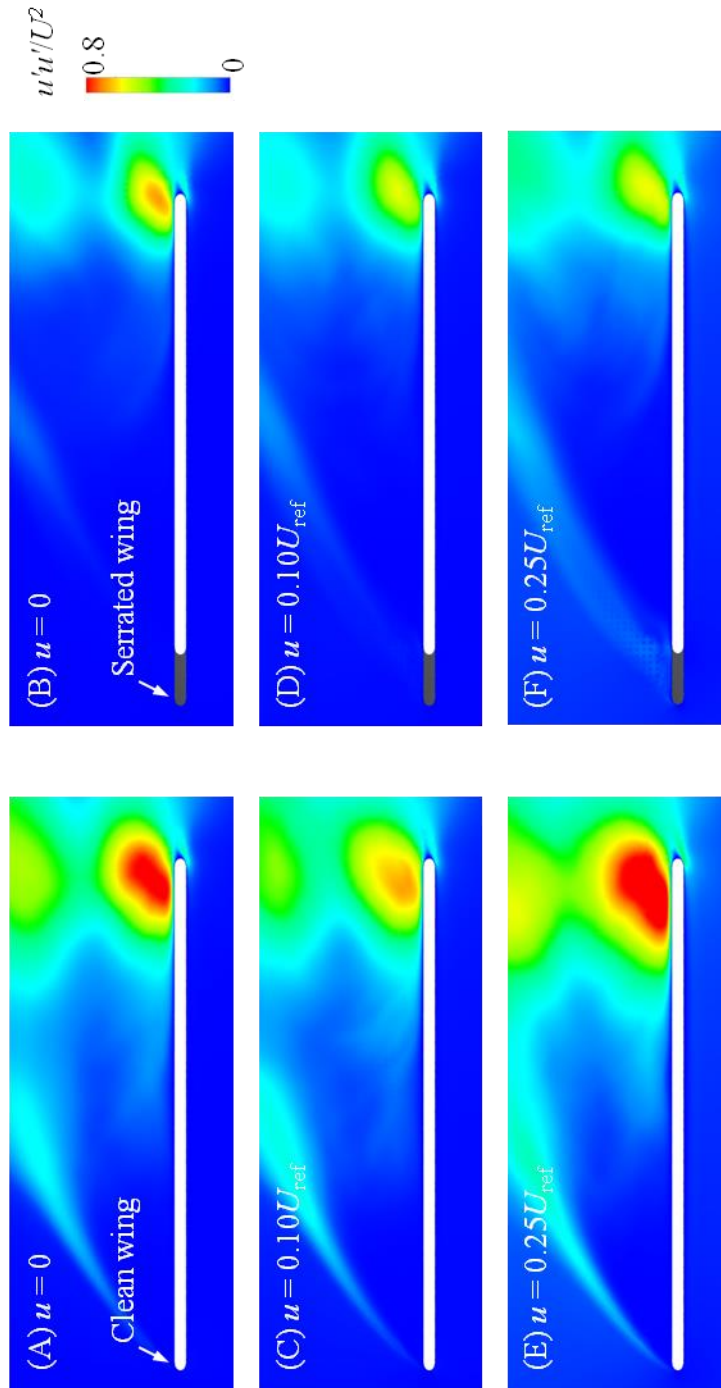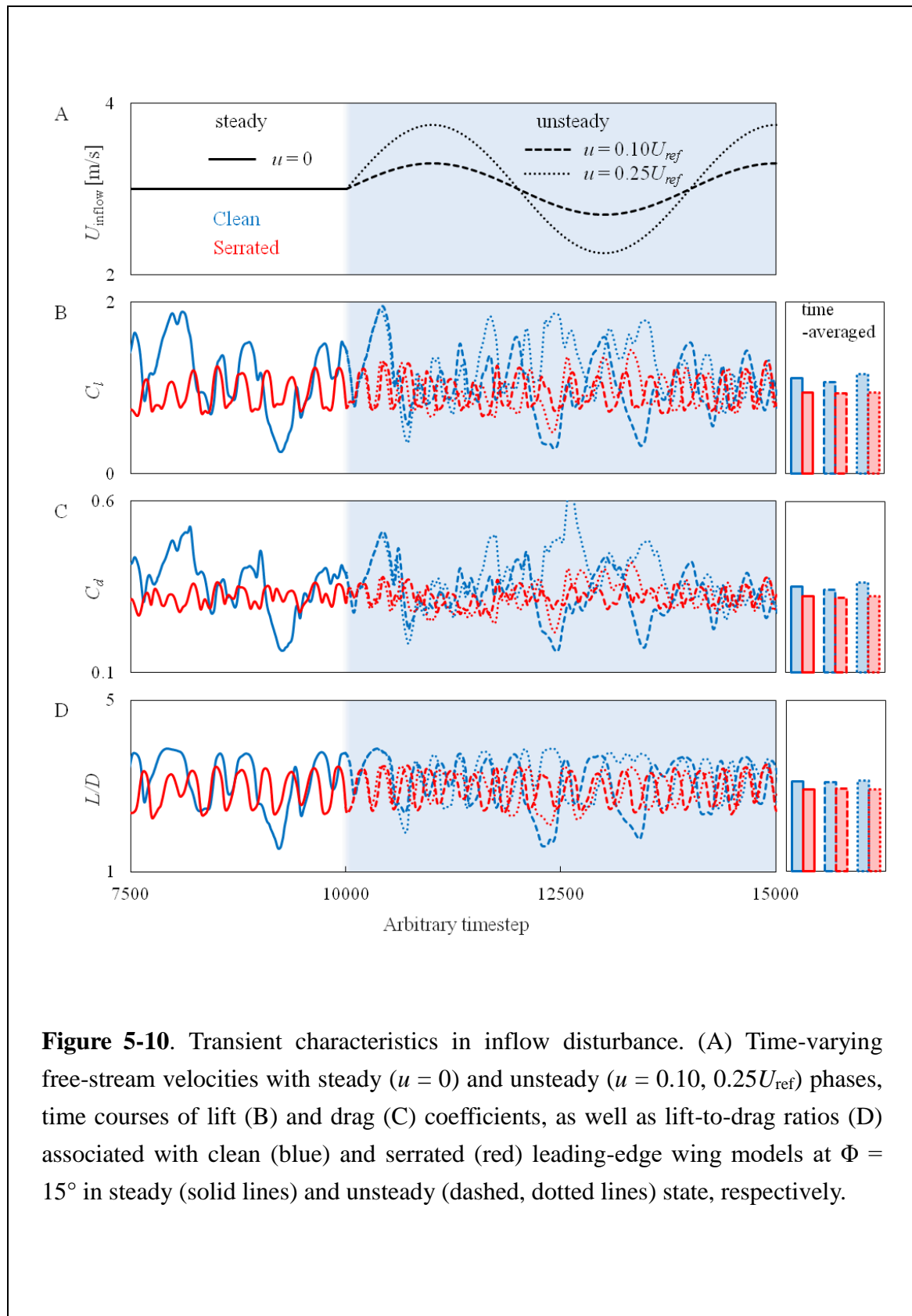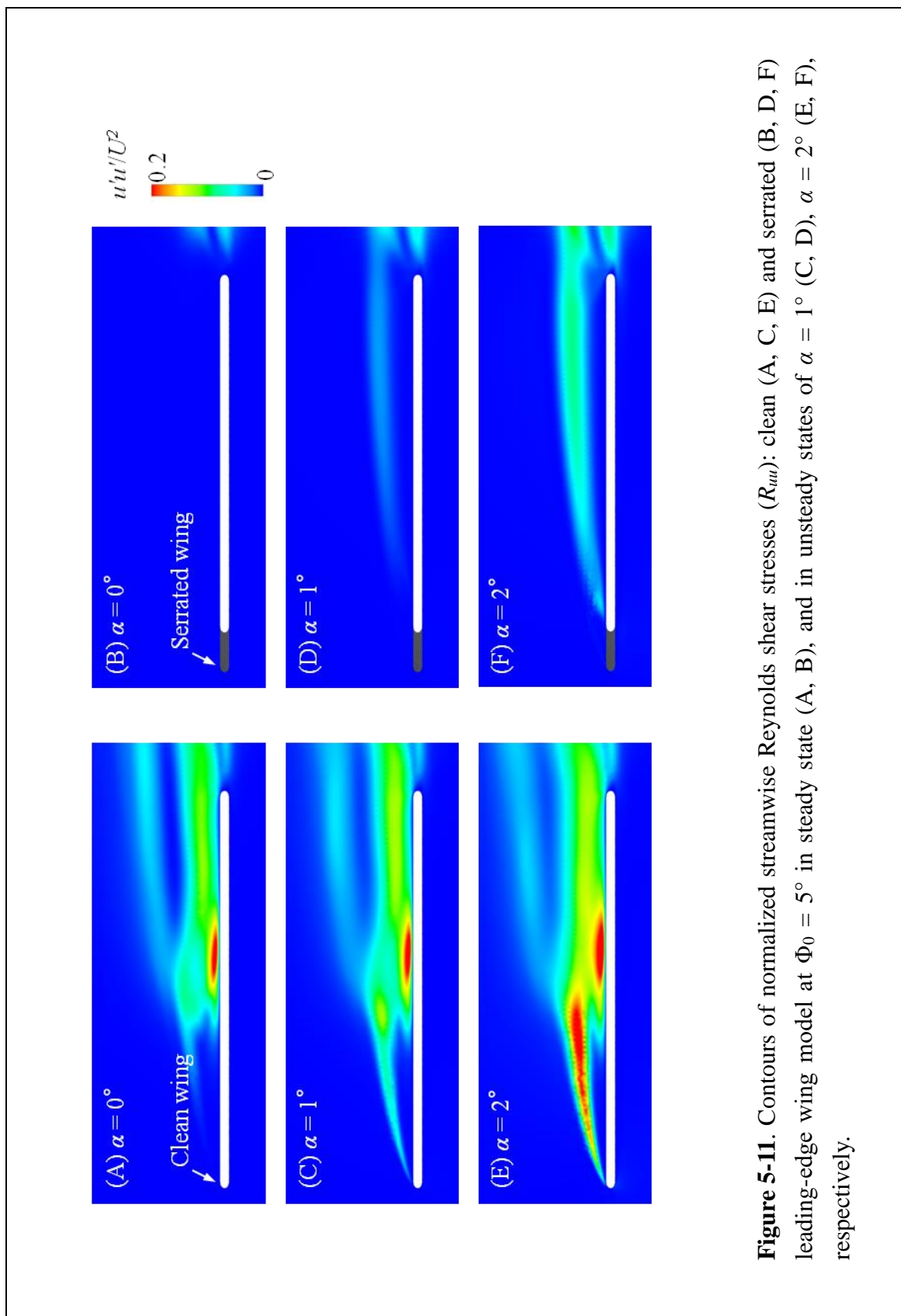
Figure 5-11. Contours of normalized streamwise Reynolds shear stresses (R_{uu}): clean (A, C, E) and serrated (B, D, F) leading-edge wing model at $\Phi_0 = 5°$ in steady state (A, B), and in unsteady states of $\alpha = 1°$ (C, D), $\alpha = 2°$ (E, F), respectively.
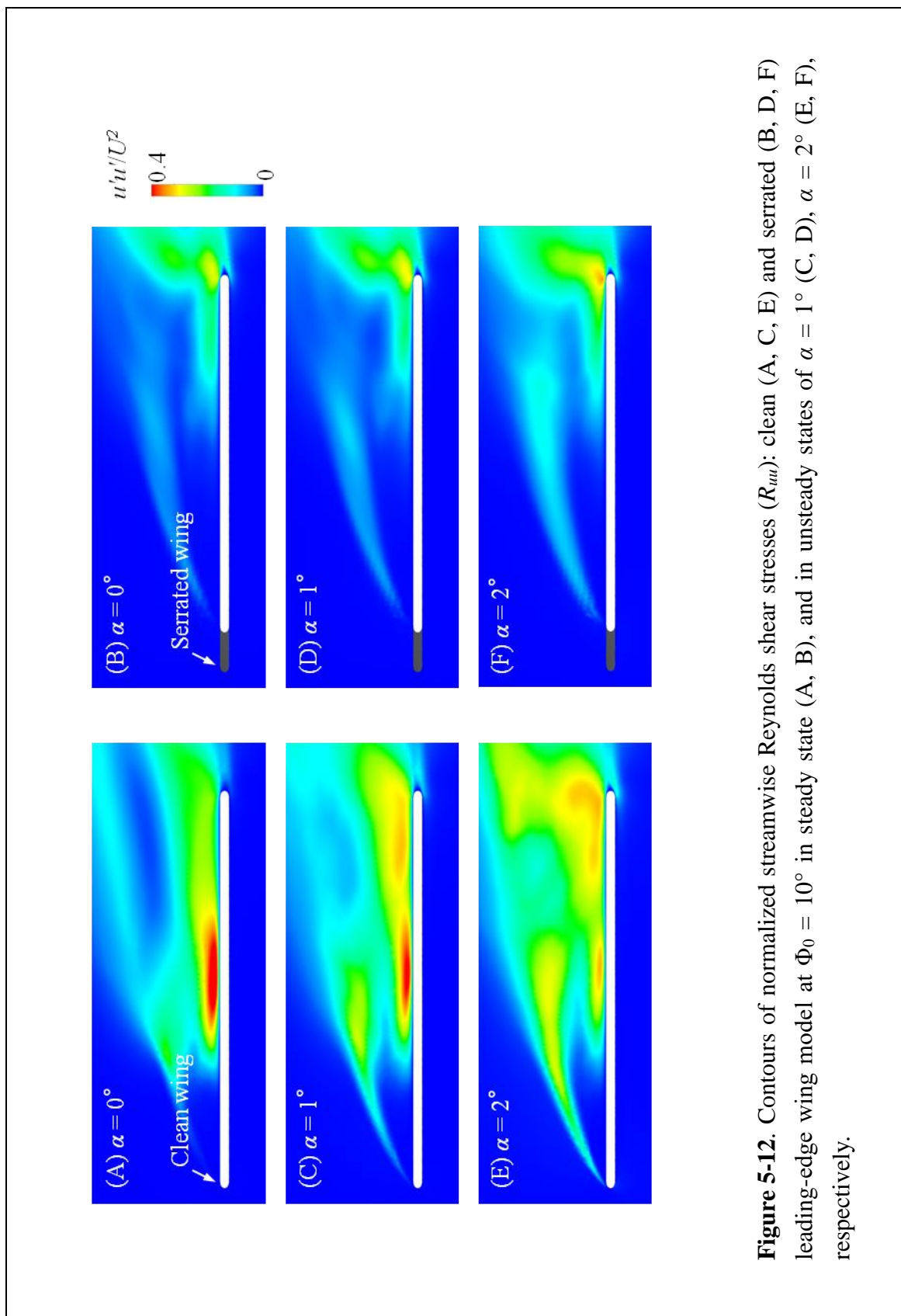
Figure 5-12. Contours of normalized streamwise Reynolds shear stresses (R_{uu}): clean (A, C, E) and serrated (B, D, F) leading-edge wing model at $\Phi_0 = 10°$ in steady state (A, B), and in unsteady states of $\alpha = 1°$ (C, D), $\alpha = 2°$ (E, F), respectively.
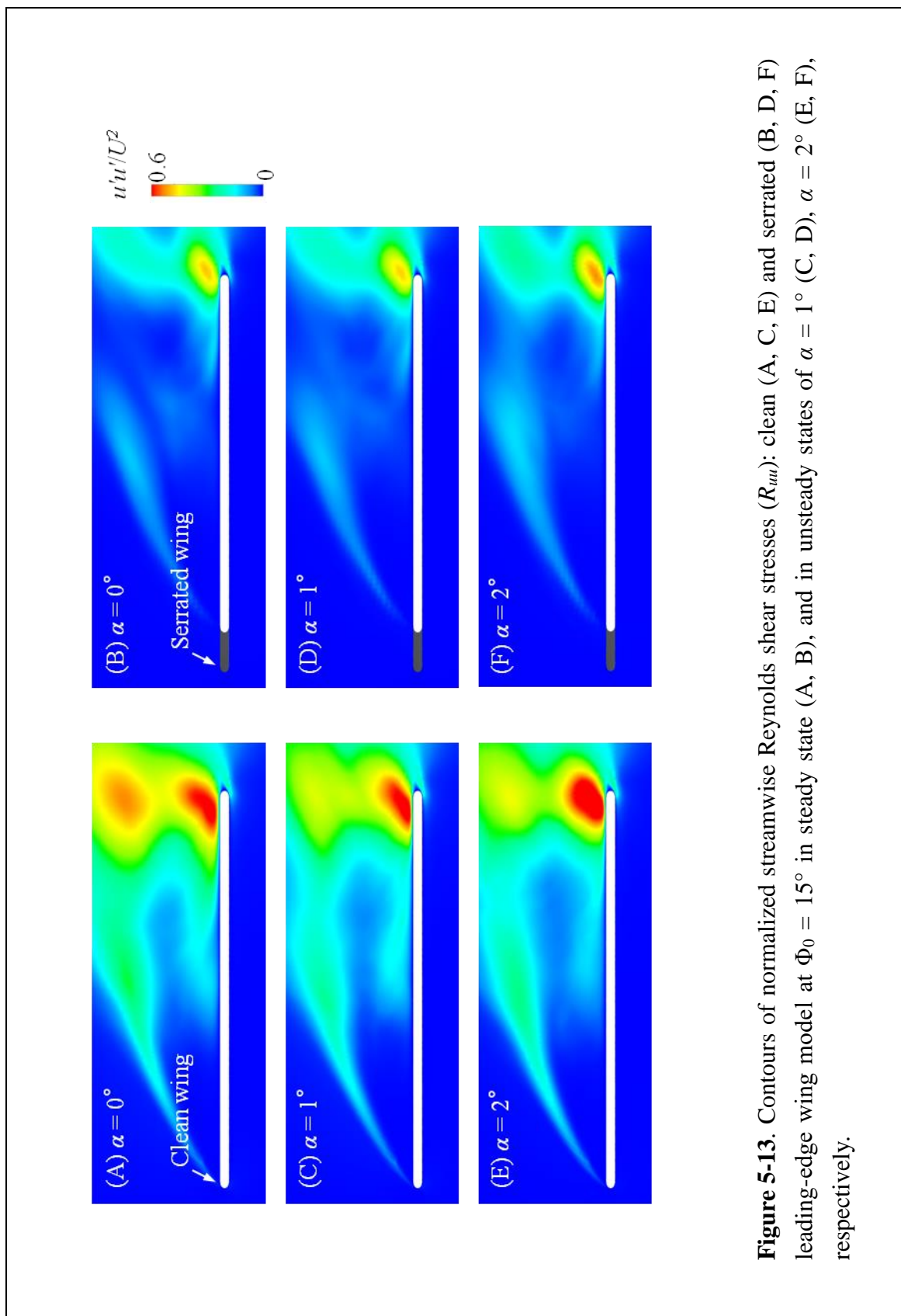
Figure 5-13. Contours of normalized streamwise Reynolds shear stresses (R_{uu}): clean (A, C, E) and serrated (B, D, F) leading-edge wing model at $\Phi_0 = 15°$ in steady state (A, B), and in unsteady states of $\alpha = 1°$ (C, D), $\alpha = 2°$ (E, F), respectively.
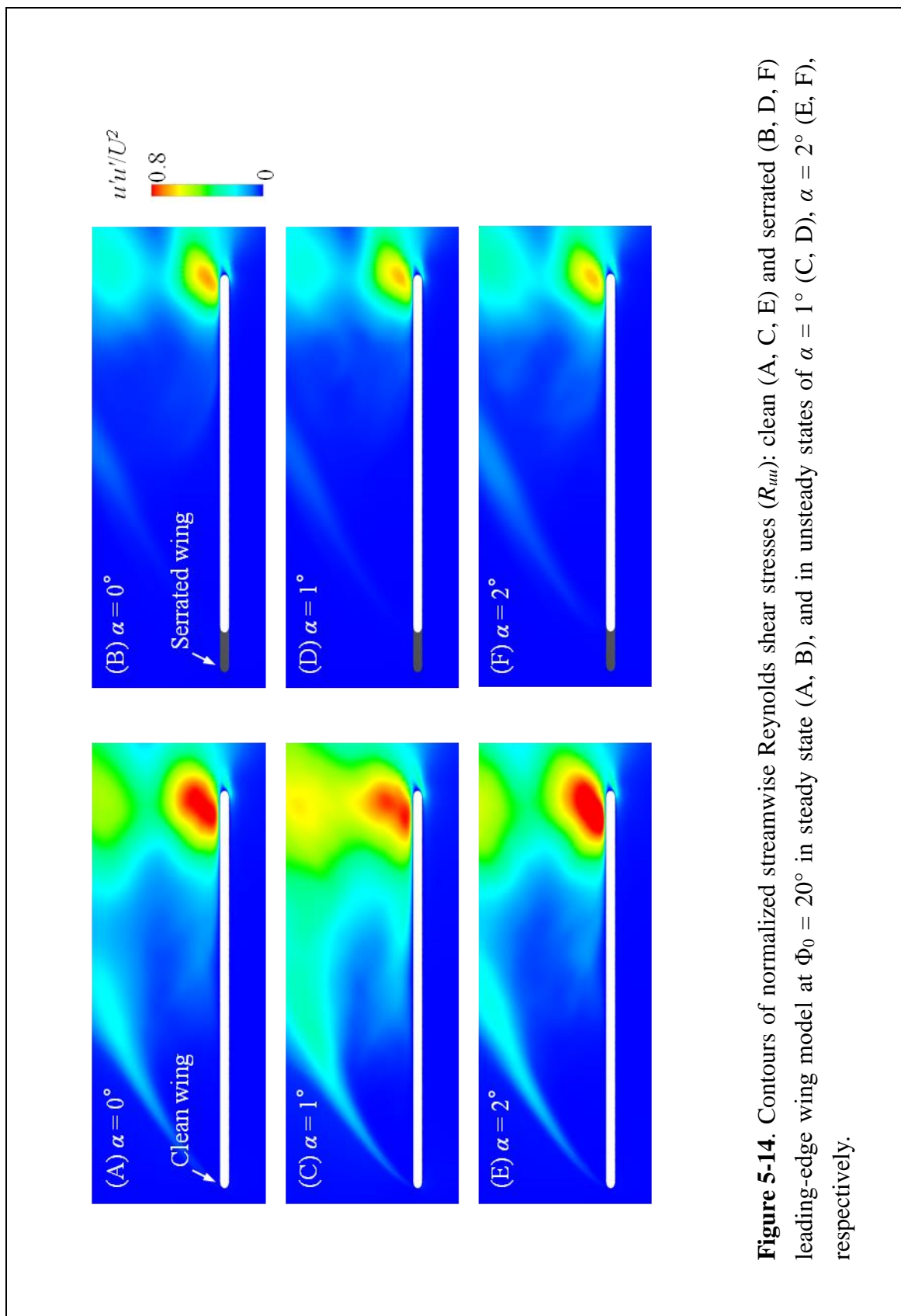
Figure 5-14. Contours of normalized streamwise Reynolds shear stresses (R_{uu}): clean (A, C, E) and serrated (B, D, F) leading-edge wing model at $\Phi_0 = 20°$ in steady state (A, B), and in unsteady states of $\alpha = 1°$ (C, D), $\alpha = 2°$ (E, F), respectively.
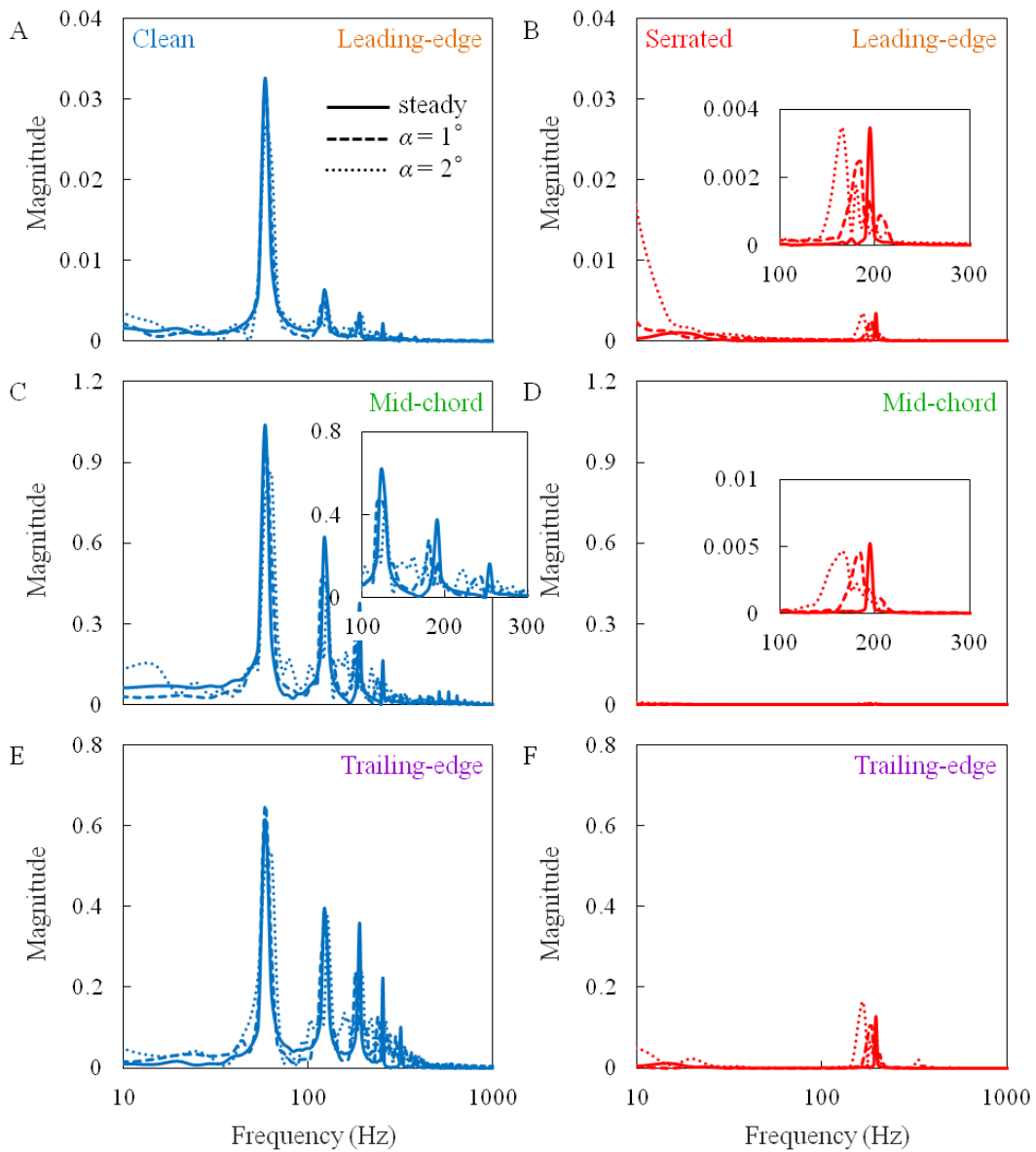
Figure 5-15. Streamwise velocity spectra at leading-edge (A, B), mid-chord (C, D), and trailing-edge (E, F) of clean (blue) and serrated (red) leading-edge wing models at $\Phi_0 = 5°$ in steady state (solid line) and with $\alpha = 1°$ (dashed line) and $\alpha = 2°$ (dotted line) in unsteady state, respectively.
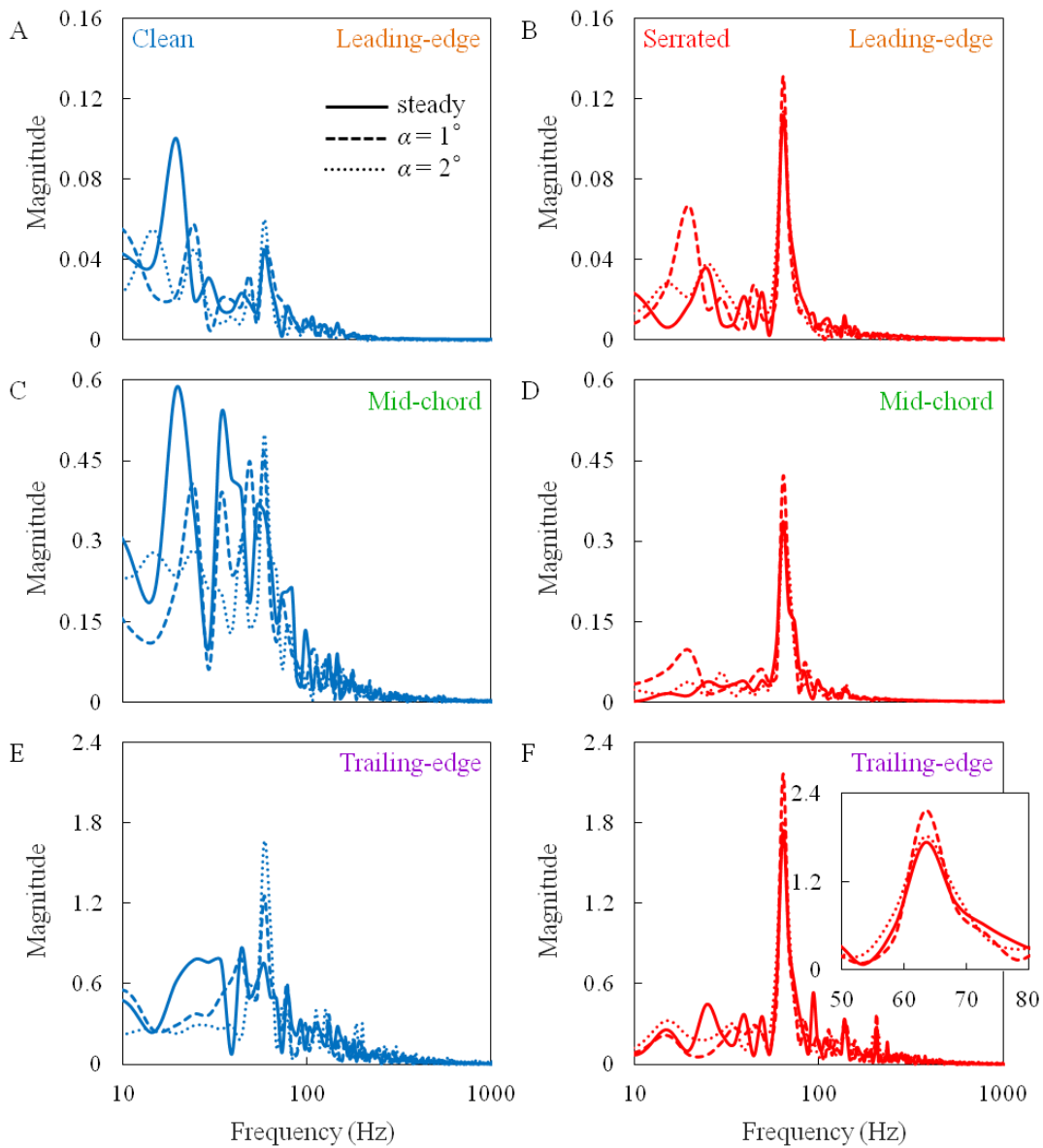
Figure 5-16. Streamwise velocity spectra at leading-edge (A, B), mid-chord (C, D), and trailing-edge (E, F) of clean (blue) and serrated (red) leading-edge wing models at $\Phi_0 = 15°$ in steady state (solid line) and with $\alpha = 1°$ (dashed line) and $\alpha = 2°$ (dotted line) in unsteady state, respectively.

Figure 5-17. Transient characteristics in pitch disturbance. (A) Time-varying pitch angles with steady ($\alpha = 0°$) and unsteady ($\alpha = 1°$, $\alpha = 2°$) phases, time courses of lift (B) and drag (C) coefficients, as well as lift-to-drag ratios (D) associated with clean (blue) and serrated (red) leading-edge wing models at $\Phi_0 = 5°$ in steady (solid lines) and unsteady (dashed, dotted lines) state, respectively.
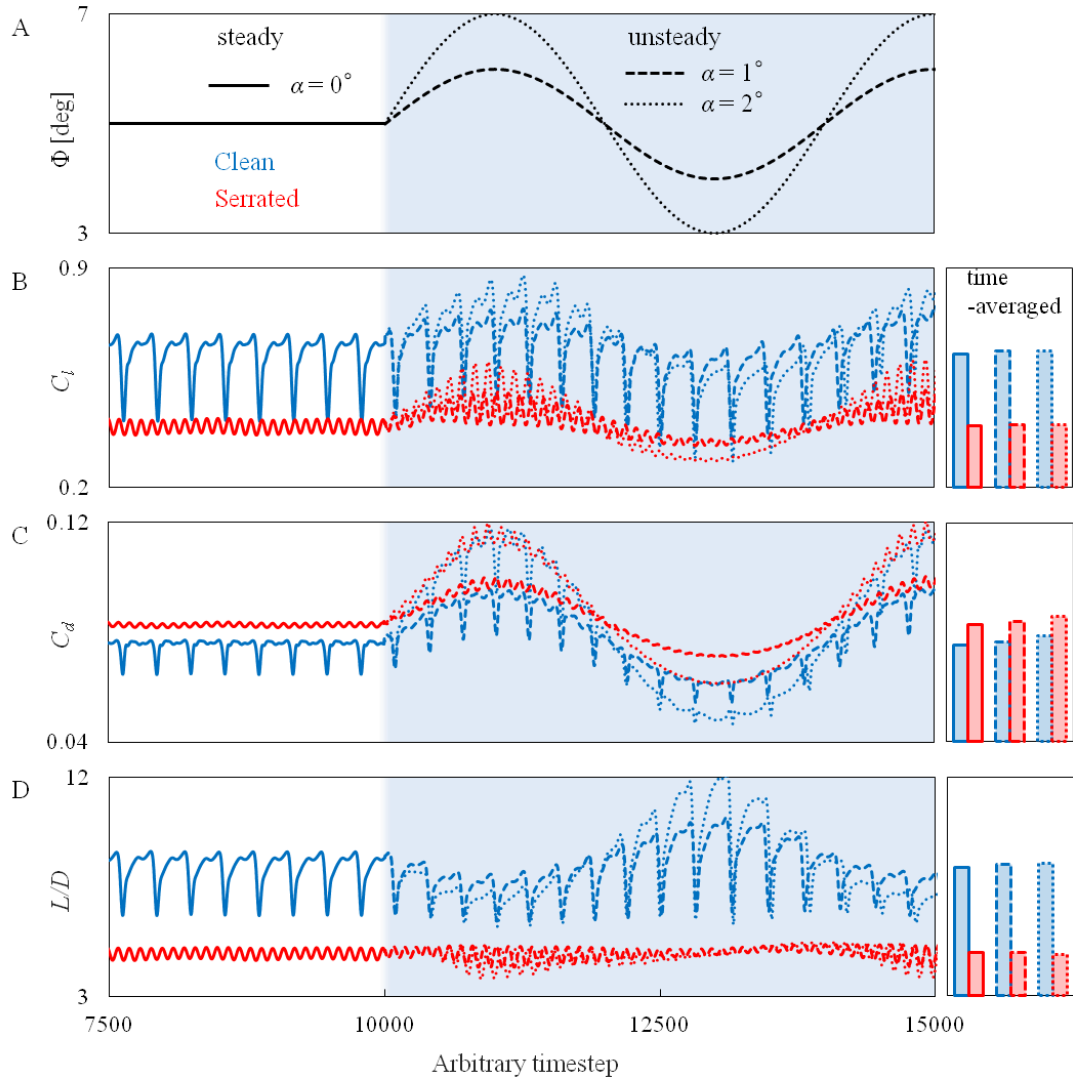
Figure 5-18. Transient characteristics in pitch disturbance. (A) Time-varying pitch angles with steady ($\alpha = 0°$) and unsteady ($\alpha = 1°$, $\alpha = 2°$) phases, time courses of lift (B) and drag (C) coefficients, as well as lift-to-drag ratios (D) associated with clean (blue) and serrated (red) leading-edge wing models at $\Phi_0 = 15°$ in steady (solid lines) and unsteady (dashed, dotted lines) state, respectively.
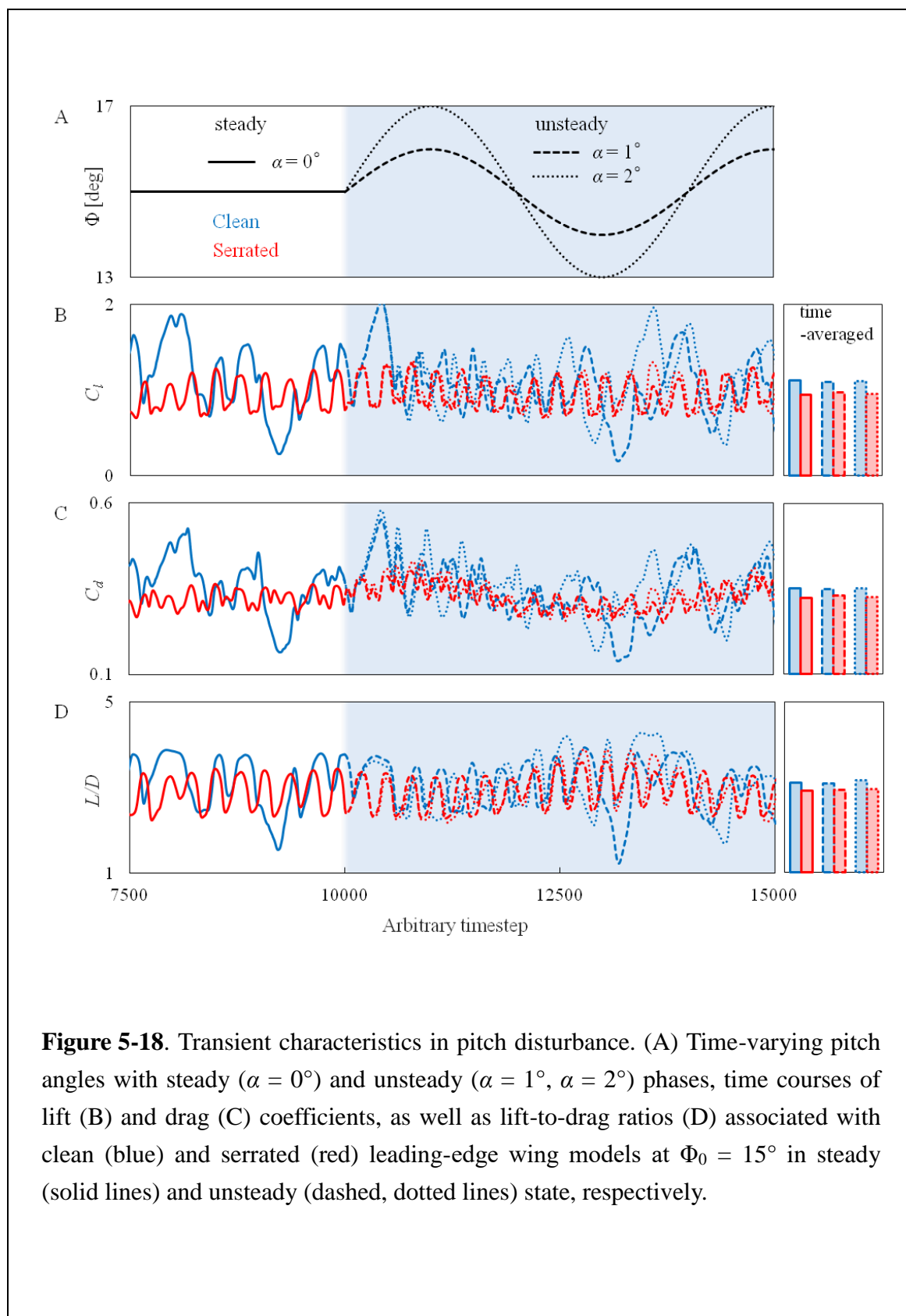
5.3.3 Unsteadiness in aerodynamic forces

Effects of gust disturbance on aerodynamic performance were further evaluated through a comparison of time-varying lift and drag coefficients (C_l, see equation 4-7; C_d, see equation 4-8), as well as lift-to-drag ratios via angles of attack between the clean and serrated wing models. Time courses of lift and drag coefficients and lift-to-drag ratios were plotted and compared in figures 5-9 and 5-10 for inflow fluctuation and in figures 5-17 and 5-18 for pitching fluctuation for both clean and serrated wing models at AoA = 5°, 15°, respectively.

5.4 Aerodynamic robustness in fluctuated inflow

Here we investigate whether the leading-edge serration-based mechanisms are of potential robustness under perturbed inflow in terms of flow separation and reattachment as well as their correlations with the aerodynamic force production of lift and drag. It is notable that the passive control mechanisms associated with laminar-turbulent transition in leading-edge serrations [10] still hold: the leading-edge serrations are in evidence capable of remarkably stabilizing the turbulent fluctuation in the fluctuated inflow over a broad range of AoAs up to 20° and hence providing robustness or gust disturbance rejection to the aerodynamic performance.

5.4.1 At lower AoAs of 5° and 10°

The clean wing model is obviously exposed to a large portion of turbulent fluctuations with a rapid laminar-turbulent transition on suction surface, followed by attached turbulent boundary layers downstream to the trailing-edge with stronger intensity (figures 5-3(A), (C), (E) and 5-4(A), (C), (E)). The intensity of the laminar-turbulent transition is significantly enhanced with increasing the inflow fluctuation up to $u = 0.25U_{ref}$, while the turbulent fluctuation turns out to be more intense from mid-chord to the trailing-edge (figures 5-3(A), (C), (E) and 5-4(A), (C), (E)). In contrast, the serrated wing model clearly demonstrates the capability to suppress the turbulent fluctuations over most portion of the upper surface with the suction-flow remained in a completely laminar state (figures 5-3(B), (D), (F) and 5-4(B), (D), (F)). This passive flow control mechanism further works effectively for the unsteady case with the two disturbed inflows. Moreover, while the large fluctuation of $u = 0.25U_{ref}$ (figure 5-3(F)) seems to leave a notable region of high streamwise Reynolds stress over

73

the upper surface at AoA of 5°, the flow separation pattern turns out to become closer at the larger AoA of 10° among the steady (figure 5-4(B)) and unsteady (figures 5-4(D), (F)) cases. This implies that the leading-edge serrations can be a robust device effectively adaptive to high angles of attack.

We further investigate the dominant frequencies of the flow fluctuations through FFT-based velocity spectrum analysis to clarify the inflow fluctuation dependency. As depicted in figure 5-7, at AoA of 5°, the velocity spectra show a pronounced difference between clean and serrated models. In the steady case, the clean model presents a highest peak at $f = 58.6$ Hz at leading-edge (figure 5-7(A)), pointing to the dominant fluctuation frequency of the separated shear layer; and several prominent peaks are also notable at mid-chord (figure 5-7(C)) and trailing-edge (figure 5-7(E), corresponding to high harmonic-frequency eddies, associated with the laminar-turbulent transition. In the unsteady case, with the enhancement of the Reyonlds stress instability owing to the perturbed inflow-induced fluctuation (5 Hz, see equation 5-1), the spectral magnitude demonstrates a remarked reduction (dashed line) with increasing the inflow velocity fluctuation or even breaking-up into two spectral prominences (dotted line) at $u = 0.25U_{ref}$ in the vicinity of leading-edge (figure 5-7(A)). Because the fluctuated shear layer then transits rapidly into turbulence and interacts with the trailing-edge vortex, the harmonic-frequency peaks in the vicinity of mid-chord (figure 5-7(C)) and trailing-edge (figure 5-7(E)) are similarly weakened and broken up, eventually transformed into a broadband spectral fluctuation, which may be referred as the source of broadband nosie.

The serrated model however obviously shows much lower magnitudes of the dominant fluctuation frequencies (solid lines) on the upper surface in the steady case, merely with a spectral prominence at $f = 195.3$ Hz (figures 5-7(B), (D) and (F)) corresponding to the shedding of trailing-edge vortices, indicating a completely laminar state of the suction flow (figure 5-3(B)). Moreover, the serrated model demonstrates a remarkable independency and robustness to the inflow fluctuation with the velocity spectra remained to the same lower level as in the steady case while showing a spectral fluctuation at frequencies ranging from 150 Hz to 250 Hz (dashed line) or 100 Hz to 300 Hz (dotted line).

While the leading-edge serrations are capable of suppressing the turbulent fluctuations and hence remarkably mitigating the aerodynamic force fluctuations (figure 5-9), the serrated model shows poor aerodynamic performance in lift coefficient as well

as in lift-to-drag ratio at a lower AoA of 5° as pointed out in Chapter 4. Interestingly, the fluctuations in aerodynamic forces turn out to be even suppressed in amplitude under inflow disturbance compared to the steady case but are notable amplified during the deceleration of the sinusoidal inflow, in particular in the serrated model (red) (figures 5-9(B), (C) and (D)), at $u = 0.25U_{\text{ref}}$ (dotted lines). This implies that the deceleration in inflow may induce some instability in the laminar-turbulent transition.

5.4.2   At higher AoAs of 15° and 20°

The clean model (see streamwise Reynolds stresses in figures 5-5(A), (C), (E) and 5-6(A), (C), (E)) is apparently very sensitive to inflow fluctuation with a notable enhanced instability within the shear layer, which interacts with the trailing-edge vortex, resulting in much more pronounced turbulent fluctuations in the vicinity of the trailing-edge. The serrated model however can effectively suppress the laminar-turbulent transition and its interplay with the trailing-edge vortex, resulting in remarked suppression of the streamwise Reynolds stress in the vicinity of trailing-edge (figures 5-5(B), (D), (F) and 5-6(B), (D), (F)), which is of high robustness at high angles of attack.

The clean model presents very complex spectra at AoA of 15°, with a feature of multiple spectral peaks at the mid-chord (figure 5-8(C)) and trailing-edge (figure 5-8(E)) in the steady case (solid line). The inflow fluctuation apparently further enhances the complexity and irregularity of the velocity spectral distributions (dashed and dotted lines), with the interactions among the fluctuated inflow, the laminar-turbulent transition, and the trailing-edge vortex. In the serrated model in the steady case (solid line), however, merely one single dominant peak is observed with the same frequency at all three feature points (figures 5-8(B), (D) and (F)), implying that the laminar-turbulent transition is successfully suppressed. Obviously this mechanism further demonstrates its capability in the fluctuated inflow, which resulted in two (dashed line) or three (dotted line) frequency prominences while reducing the dominant spectral magnitudes significantly. This corresponds with the distribution of streamwise Reynolds stresses (figure 5-5(B), (D) and (F)) that the turbulent fluctuation in the vicinity of trailing-edge slightly mitigates under perturbation.

The aerodynamic force production at AoA of 15° (figure 5-10) in the serrated model demonstrates potential robustness: suppressing the turbulent fluctuations while

achieving an equivalent aerodynamics performance compared to the clean model in terms of lift coefficient and lift-to-drag ratio but with significantly reduced fluctuations in amplitude. Moreover, there seemingly exists seldom discrepancy between the two fluctuated inflows of $u = 0.1U_{\text{ref}}$, $0.25U_{\text{ref}}$ as well as in the acceleration and deceleration phases of the sinusoidal inflow waveform.

5.5 Aerodynamic robustness in fluctuated wing motion

Here we further give an investigation on the aerodynamic robustness of the leading-edge serrations in fluctuated pitch-motion in terms of streamwise Reynolds stress, velocity spectra as well as lift and drag coefficients and lift-to-drag ratios. It is confirmed that the leading-edge serrations also demonstrates the capability of vertical disturbance rejection to the perturbed pitch motion over a broad range of AoAs up to 20°.

5.5.1 At lower AoA$_{initial}$ of 5° and 10°

As illustrated in figures 5-11 and 5-12, while the pitch fluctuation results in enhancement of the turbulent instability within the separated shear layer, particularly at the higher pitching fluctuation of $\alpha = 2°$, interestingly the serrated model obviously led to a similar flow patterns as in the case of inflow fluctuation. The leading-edge serrations also work effectively to suppress the turbulent fluctuations over most portion of the upper surface with the suction-flow remained in a completely laminar state (figures 5-11(B), (D), (F) and 5-12(B), (D), (F)). The velocity spectra further provide evidence: the disturbed shear layer excites a broadband spectral fluctuation (figures 5-15(C) and (E)) at $\alpha = 2°$ (dotted) in the clean model; the serrated model demonstrates remarked independency to the pitching disturbance with the velocity spectra remained to the same lower level as in the steady case while showing a slight shift of the dominant peak to the lower side (figures 5-15(B), (D) and (F)).

5.5.2 At higher AoA$_{initial}$ of 15° and 20°

As shown in figures 5-13 and 5-14, the streamwise Reynolds stress distributions show less discrepancy between steady and unsteady cases in both clean and serrated models. The velocity spectra (figures 5-16) however still present pronounced differences in the clean model between steady (solid lines) and unsteady (dashed and

dotted lines) cases while in the serrated model the spectral distributions show remarked robustness in response to the pitch fluctuation (figures 5-16(B), (D) and (F)).

5.5.3 Aerodynamic performance

As illustrated in figures 5-17 and 5-18, while the leading-edge serrations are capable of mitigating the aerodynamic force fluctuations over a broad range of AoAs up to 20° even under dynamic pitching, the tradeoff between passive turbulence control (i.e. noise suppression) and force production still exists: lower lift coefficient and lift-to-drag ratio at $AoA_{initial}$ of 5° (figures 5-17(B) and (D)) but an even aerodynamic performance at $AoA_{initial}$ of 15° (figures 5-18(B), (C) and (D)) compared to the clean model. In addition, while the sinusoidal pitch-motion is observed to apparently result in a periodic feature of aerodynamic forces pronouncedly in the clean model, the serrated model is of potential robustness in lift-to-drag ratio at both lower and higher $AoA_{initial}$ (figures 5-17(D) and 5-18(D)). This implies that the capability of achieving both noise suppression and aerodynamic performance in leading-edge serrations is of highly potential robustness to the vertical fluctuation.

5.6 Summary

Motivated by the sophisticated silent flight of owls that can achieve remarkable maneuvering while aeroacoustic control under complex turbulent environments, we have conducted a computational study of aerodynamic robustness in owl-inspired leading-edge serrations by means of LES-based modeling of single-feather clean and serrated wing models. The CFD modeling was validated through a mesh independence study and a comprehensive comparison with PIV measurements in Chapter 4. Two conceptual wind-gust models were employed to mimic a horizontal disturbance in free-stream inflow and a vertical disturbance in pitch angle over a broad range of angles of attack (AoAs) over $0° \leqslant \Phi \leqslant 20°$, which were both implemented in a form of sinusoidal fluctuations.

Our results indicate that the leading-edge serration-based passive control mechanisms associated with the laminar-turbulent transition still hold under perturbed inflow and pitch motion, and are of potential robustness in aerodynamic performance.

(1) Under the sinusoidal inflow fluctuation, the serrated model is capable of

dynamically suppressing the turbulent and aerodynamic force fluctuations but pays a cost in lowering the lift coefficients and lift-to-drag ratios at a lower AoA = 5° but at a higher AoAs > 15° it is of potential robustness in achieving an equivalent aerodynamic performance compared to the clean model with largely reduced fluctuations in amplitude.

(2) Under the sinusoidal pitching fluctuation, the serrated model demonstrates the capability of achieving similar aerodynamic robustness as observed in the fluctuated inflow while suppressing the pitch-induced fluctuating characteristic in aerodynamic force production.

(3) The tradeoff between turbulent flow control, i.e. aeroacoustic suppression and force production in the serrated model is confirmed independently to the wind-gust conditions.

It should be mentioned that, for simplicity, in this study we have idealized realistic wind-gust conditions by proposing two conceptual models with consideration of fluctuations in horizontal and vertical directions. We further neglected the realistic 3D shape of the serrations, as well as other morphological characteristics such as trailing-edge fringes and velvety surfaces as well as the feather flexibility, which may work complimentarily in passive flow control and aeroacoustic suppression of serrated wings under wind-gust. An integrated study on aerodynamic robustness in owl-inspired leading-edge serrations in a von-Karman vortex wake as well as realistic 3D modeling of owl wings undergoing realistic flapping is our next task to uncover how owls are capable of achieving the sophisticated silent flight in realistic turbulent environments.

References

[1] Graham RR 1934 The silent flight of owls. *Journal of the Royal Aeronautical Society*. **38** 837-843. (http://dx.doi.org/10.1017/S0368393100109915)

[2] Gruschka HD, Borchers IU and Coble JG 1971 Aerodynamic noise produced by a gliding owl. *Nature*. **233** 409-411. (http://dx.doi.org/10.1038/233409a0)

[3] Kroeger RA, Grushka HD and Helvey TC 1972 Low speed aerodynamics for ultra-quiet flight. *Final Technical Report (July 1970 – May 1971) Tennessee Univ Space Inst Tullahoma* (http://www.dtic.mil/docs/citations/AD0893426)

[4] Lilley GM 1998 A study of the silent flight of the owl. *4th AIAA/CEAS Aeroacoustics Conference, Toulouse, AIAA Paper*. **2340** 1-6. (http://dx.doi.org/10.2514/6.1998-2340)

[5] Chen K, Liu Q, Liao G, Yang Y, Ren L, Yang H and Chen X 2012 The sound suppression characteristics of wing feather of owl (*Bubo bubo*). *Journal of Bionic Engineering*. **9** 192-199. (http://dx.doi.org/10.1016/S1672-6529(11)60109-1)

[6] Wagner H, Weger M, Klaas M and Schröder W 2017 Features of owl wings that promote silent flight. *Interface Focus* **7** 20160078. (http://dx.doi.org/10.1098/rsfs.2016.0078)

[7] Sarradj E, Fritzsche C and Geyer T 2011 Silent owl flight: Bird flyover noise measurements. *AIAA Journal*. **49** 769-779. (http://dx.doi.org/10.2514/1.J050703)

[8] Geyer T, Sarradj E and Fritzsche C 2012 Silent owl flight: Acoustic wind tunnel measurements on prepared wings. *18th AIAA/CEAS Aeroacoustics Conference (33rd AIAA Aeroacoustics Conference), Colorado Springs, AIAA Paper*. **2230** 1-17. (http://dx.doi.org/10.2514/ 6.2012-2230)

[9] Geyer T, Claus VT, Sarradj E and Markus PM 2016 Silent owl flight: The effect of the leading edge comb on the gliding flight noise. *22nd AIAA/CEAS Aeroacoustics Conference, Lyon, AIAA Paper*. **3017** 1-12. (http://dx.doi.org/10.2514/6.2016-3017)

[10] Rao C, Ikeda T, Nakata T and Liu H 2017 Owl-inspired leading-edge serrations play a crucial role in aerodynamic force production and sound suppression. *Bioinspiration and Biomimetics*. **12** 1-13. (http://dx.doi.org/10.1088/1748-3190/aa7013)

[11] Ikeda T, Ueda T, Nakata T, Noda R, Tanaka H, Fujii T and Liu H 2018 Morphology effects of leading-edge serrations on aerodynamic force production: an integrated study using PIV and force measurements. *Journal of Bionic Engineering*. **15** 661-672. (http://doi.org/10.1007/s42235-018-0054-4)

[12] Shepard ELC, Ross AN, Portugal SJ 2016 Moving in a moving medium: new perspectives on flight. *Phil. Trans. R. Soc. B* **371** 1-7. (http://dx.doi.org/10.1098/rstb.2015.0382)

[13] Wolf T and Konrath R 2015 Avian wing geometry and kinematics of a free-flying barn owl in flapping flight. *Experiments in Fluids*. **56**. (http://dx.doi.org/10.1007/s00348-015-1898-6)

[14] Ortega-Jimenez VM, Badger M, Wang H, Dudley R 2016 Into rude air: hummingbird flight performance in variable aerial environments. *Phil. Trans R. Soc. B* **371** 1-7. (http://dx.doi.org/10.1098/rstb.2015.0387)

6. Conclusion remarks and future work

In this study, motivated by the sophisticated silent flight of owls that can achieve remarkable maneuvering while aeroacoustic control under turbulent environments, we conducted an integrated study by combining LES-based simulations and low-speed wind tunnel experiments on highly unsteady flows associated with laminar-turbulent transition around owl-inspired single-feather wing models with and without leading-edge serrations. The CFD modeling was validated through mesh independence study and a comprehensive comparison with PIV measurements in the wind tunnel.

6.1 The mechanisms of leading-edge serrations in aeroacoustic noise suppression

As our first step to investigate the essential mechanisms of the leading-edge serrations in steady flow condition, we pay specific attention to the aerodynamic characteristics of the wing models under uniform incoming flow. A broad range of angles of attack (AoAs) over 0° to 20° was taken into consideration based on the measurements by Wolf et al. [1] in which the effective angle of attack was observed to range from -20° to 20° in flapping flights of barn owls.

Based on the simulated results, we find that the serrated wing model can passively control the laminar-turbulent transition to suppress the high frequency eddies, and hence leads to sound suppression. This mechanism is likely achieved by the leading-edge serrations, which, as a flow filter, break up the leading-edge vortex into numbers of small eddies and hence suppress the KH instability within the separated shear layer. Moreover, the leading-edge serrations seems to be capable of providing a strategy in resolving the tradeoff between sound suppression and force production. Compared to the clean wing model, the serrated wing model pays a cost of lowering aerodynamic performance to achieve sound suppression at lower AoAs < 15° but is capable to achieve both sound suppression and an even aerodynamic performance at higher AoAs > 15° where owl wings often reach at in flight [1].

6.2 Aerodynamic robustness in owl-inspired leading-edge serrations

In order to further investigate the aerodynamic robustness in owl-inspired

leading-edge serrations, two conceptual wind-gust models were further employed to mimic a horizontal disturbance in free-stream inflow and a vertical disturbance in pitch angle, which were both implemented in a form of sinusoidal fluctuations.

Our results indicate that the leading-edge serrations are of potential robustness in aerodynamic performance. The serrated model is capable of dynamically suppressing the turbulent and aerodynamic force fluctuations under perturbed inflow and fluctuated pitch motion. Furthermore, the tradeoff between aeroacoustic noise suppression and aerodynamic force production in the serrated model is confirmed independently to the wind-gust conditions.

In general, based on this study, it is revealed that the owl-inspired leading-edge serrations can be a robust micro-device for aeroacoustic control coping with unsteady and complex wind environments in biomimetic rotor designs for various fluid machineries.

6.3 Further works

It should be mentioned that, for simplicity, in this study we have idealized realistic wind-gust conditions by proposing two conceptual models with consideration of fluctuations in horizontal and vertical directions. We further neglected the realistic 3D shapes of the serrations, as well as other morphological characteristics such as trailing-edge fringes and velvety surfaces as well as the feather flexibility, which may work complimentarily in passive flow control and aeroacoustic suppression of serrated wing under wind-gust. An integrated study on aerodynamic robustness in owl-inspired leading-edge serrations in a von-Karman vortex wake as well as realistic 3D modeling of owl wings undergoing realistic flapping is our next task to uncover how owls are capable of achieving the sophisticated silent flight in realistic turbulent environments. Furthermore, we will explore practical applications of the owl wing-inspired robust micro-devices as a biomimetic design for flow control and noise suppression in wind turbines, aircrafts, multi-rotor drones as well as other fluid machineries.

82

References

[1] Wolf T and Konrath R 2015 Avian wing geometry and kinematics of a free-flying barn owl in flapping flight. *Experiments in Fluids*. **56**. (http://dx.doi.org/10.1007/s00348-015-1898-6)

Acknowledgments

First and foremost, I would like to express the deepest gratitude to my supervisor, Professor Hao Liu, for accepting me to be his student in Chiba University and helping me get the financial support from Japanese Government MEXT scholarship. He led me into the world of Biomechanics and introduced to me my research project about the silent flight of owls which is lovely and interesting, but also full of challenges. His intelligent and inspirational guidance provides me with lots of assistance to overcome one and another academic difficulty, and encourages me to get through my depressed times. He carefully revised the manuscripts with great patience especially after being rejected first time, which is very much helpful. It is a great honor for me to study and research under his supervision. And I must say that I have gained so much from him these years, not only knowledge but also how to become a better person.

My sincere thanks go to Dr. Toshiyuki Nakata and Dr. Teruaki Ikeda, co-authors of my first paper, for their significant contributions to the manuscript. I would also like to acknowledge Dr. Hiroto Tanaka and Dr. Dmitry Kolomenskiy for valuable discussions and suggestions during lab seminars. The article published last year in Bioinspiration & Biomimetics has been selected to be part of the journal's Highlights of 2017 collection. This could not have been achieved without the help and contributions from all of them. And I am looking forward to more and more achievements in the future.

It has been a fascinating experience in my life to spend the past years living and studying in Chiba. I am sincerely grateful to all the current and past members of "Liu lab" that I met and worked with, especially Takashi Fujiwara and Dr. Ryusuke Noda who always ready to give their warmest welcome and greatest help to make my life in Japan much easier and full of enjoyment. I appreciate the moments of happiness that we get along with each other.

As a super lover of opera and classical music, I also want to express my respect and thanks to the greatest composers, Ludwig van Beethoven, Richard Wagner, Giuseppe Verdi, Gioachino Rossini, Anton Bruckner...for their opera or orchestral works that have always encourage me and make my life full of colors and excitement. Here I also would like to pay my tribute to the memory of Claudio Abbado, the most respectful musician that I admire, not only for his great interpretation of music but also his

kindness and generosity. I am so lucky to have attended his concert in 2009 and 2012, the music and those memories will never be forgotten. Sadly he is no more with us and has been together with those composers since January 20th, 2014. But he and his generosity will surely be missed forever.

Last but not least, special thanks go to my dearest Mom and Dad for their over 30 years of endless and unconditional love and support. I am never good at express the feelings, for example saying "I love you". But from the deep inside of my heart, I wish all the best to our family! And I hope I have made you proud.

<div align="right">

Chen RAO

Chiba University
2018-11

</div>